remote sensing

MDPI

Article

Synergistic Use of Hyperspectral UV-Visible OMI and Broadband Meteorological Imager MODIS Data for a Merged Aerosol Product

Sujung Go [1,2], Jhoon Kim [1,*], Sang Seo Park [3], Mijin Kim [1,4,5], Hyunkwang Lim [1], Ji-Young Kim [6], Dong-Won Lee [6] and Jungho Im [3]

1 Department of Atmospheric Sciences, Yonsei University, Seoul 03722, Korea; sujung.go@nasa.gov (S.G.); mijin.kim@nasa.gov (M.K.); raul105@yonsei.ac.kr (H.L.)
2 Joint Center for Earth Systems Technology, University of Maryland Baltimore County, Baltimore, MD 21250, USA
3 School of Urban and Environmental Engineering, Ulsan National Institute of Science and Technology, Ulsan 44919, Korea; sangseopark@unist.ac.kr (S.S.P.); ersgis@unist.ac.kr (J.I.)
4 Universities Space Research Association (USRA), Columbia, MD 21046, USA
5 NASA Goddard Space Flight Center (GSFC), Greenbelt, MD 20771, USA
6 National Institute of Environmental Research (NIER), Incheon 22689, Korea; jykim77@korea.kr (J.-Y.K.); ex12@korea.kr (D.-W.L.)
* Correspondence: jkim2@yonsei.ac.kr; Tel.: +82-2-2123-5682; Fax: +82-2-365-5163

Received: 28 September 2020; Accepted: 1 December 2020; Published: 5 December 2020

Abstract: The retrieval of optimal aerosol datasets by the synergistic use of hyperspectral ultraviolet (UV)–visible and broadband meteorological imager (MI) techniques was investigated. The Aura Ozone Monitoring Instrument (OMI) Level 1B (L1B) was used as a proxy for hyperspectral UV–visible instrument data to which the Geostationary Environment Monitoring Spectrometer (GEMS) aerosol algorithm was applied. Moderate-Resolution Imaging Spectroradiometer (MODIS) L1B and dark target aerosol Level 2 (L2) data were used with a broadband MI to take advantage of the consistent time gap between the MODIS and the OMI. First, the use of cloud mask information from the MI infrared (IR) channel was tested for synergy. High-spatial-resolution and IR channels of the MI helped mask cirrus and sub-pixel cloud contamination of GEMS aerosol, as clearly seen in aerosol optical depth (AOD) validation with Aerosol Robotic Network (AERONET) data. Second, dust aerosols were distinguished in the GEMS aerosol-type classification algorithm by calculating the total dust confidence index (TDCI) from MODIS L1B IR channels. Statistical analysis indicates that the Probability of Correct Detection (POCD) between the forward and inversion aerosol dust models (DS) was increased from 72% to 94% by use of the TDCI for GEMS aerosol-type classification, and updated aerosol types were then applied to the GEMS algorithm. Use of the TDCI for DS type classification in the GEMS retrieval procedure gave improved single-scattering albedo (SSA) values for absorbing fine pollution particles (BC) and DS aerosols. Aerosol layer height (ALH) retrieved from GEMS was compared with Cloud-Aerosol Lidar with Orthogonal Polarization (CALIOP) data, which provides high-resolution vertical aerosol profile information. The CALIOP ALH was calculated from total attenuated backscatter data at 1064 nm, which is identical to the definition of GEMS ALH. Application of the TDCI value reduced the median bias of GEMS ALH data slightly. The GEMS ALH bias approximates zero, especially for GEMS AOD values of >~0.4 and GEMS SSA values of <~0.95. Finally, the AOD products from the GEMS algorithm and MI were used in aerosol merging with the maximum-likelihood estimation method, based on a weighting factor derived from the standard deviation of the original AOD products. With the advantage of the UV–visible channel in retrieving aerosol properties over bright surfaces, the combined AOD products demonstrated better spatial data availability than the original AOD products, with comparable accuracy. Furthermore, pixel-level error analysis of GEMS AOD data indicates improvement through MI synergy.

Keywords: aerosol; remote sensing; UV-visible; merged product; meteorological imager

1. Introduction

Atmospheric aerosol monitoring by active and passive satellite sensors has been undertaken globally since 1972 [1–3] due to the significant impact of aerosols on Earth's climate system, both directly and indirectly [4]. Due to the high temporospatial variability of atmospheric aerosols and their short residence times, there is a high demand for global aerosol monitoring using both low (LEO; see Appendix A for acronyms) and geostationary (GEO) Earth orbit satellite measurements. Essential climate variables (ECVs) derived by the Global Climate Observing System (GCOS) in 2016 contribute critically to the characterization of Earth's climate. The ECVs of atmospheric aerosols include aerosol optical depth (AOD), single-scattering albedo (SSA), and aerosol layer height (ALH).

Requirements for atmospheric aerosol products include the following: Data intervals should be <4 h with a spatial resolution of 5–10 km and uncertainties of <10%, <0.03, and <1 km for AOD, SSA, and ALH, respectively. Aerosol products derived from GEO satellites that are upcoming or in use, such as the Tropospheric Emissions Monitoring of Pollution (TEMPO), Sentinel-4, Geostationary Environment Monitoring Satellite (GEMS), Advanced Geostationary Radiation Imager (AGRI), Advanced Himawari Imager (AHI), Advanced Baseline Imager (ABI), and Advanced Meteorological Imager (AMI) systems [5–11] have the potential to satisfy AOD, SSA, and ALH ECV requirements.

Although atmospheric-aerosol data can be provided by GEO satellites with a higher temporospatial resolution, aerosol products from GEO satellites are not identical in terms of product quality, temporospatial resolution, or spatial coverage, owing to differences in observation geometry and instrument characteristics including observation time, spatial resolution, channels, spectral response, signal to noise ratio (SNR), and measurement technique. Even with the same instrument data, retrieved products may have different characteristics because of the different aerosol retrieval algorithms involved.

Previous studies have investigated the synergistic use of satellite instruments for improving retrieved aerosol data [12–25] with two general aims: (1) improvement of aerosol retrieval products (e.g., SSA, ALH, and aerosol type classification) by the synergistic use of different instruments; (2) creation of 'best' AOD datasets by merging individual AOD products to provide users with optimum AOD data for points with synchronous multiple satellite observations, with improved spatial coverage.

The Aura Ozone Monitoring Instrument (OMI) ultraviolet (UV) aerosol index (UVAI) and Moderate Resolution Imaging Spectroradiometer (MODIS) fine mode fraction (FMF) were applied by Kim et al. [12] to improve aerosol retrieval products through synergistic use of individual satellite instruments to classify aerosol types as carbonaceous, dust, sea-salt, or sulfate. A-train Atmospheric InfraRed Sounder (AIRS) carbon monoxide (CO) data were used by Torres et al. [13] as a tracer of smoke aerosols to separate carbonaceous and dust aerosols in the OMI operational aerosol (OMAERUV) algorithm. They also produced aerosol height climatological data from A-train Cloud-Aerosol Lidar with Orthogonal Polarization (CALIOP) data to calculate UV AOD and SSA values with the same algorithm. Vermote et al. [14] retrieved surface reflectance data from multi-angle imaging spectroradiometer (MISR) data by the synergistic application of MODIS AOD data, and retrieved MISR SSA data for haze aerosols. Jeong and Hsu [16] retrieved aerosol height data for smoke by the synergistic use of MODIS, OMI, and CALIOP with A-train constellations. CALIOP provides accurate (30–60 m vertical resolution in the troposphere [16]) aerosol-layer altitudinal data that cannot be obtained from nadir-view satellites, and this aerosol height data aided calculation of SSA in CALIOP paths, and also the prediction of aerosol heights where there is no CALIOP path. Moreover, by considering a spheroidal model for dust particles, Lee et al. [17] retrieved aerosol heights for both smoke and dust by the synergistic use of the Visible–Infrared (IR) Imaging Radiometer Suite (VIIRS), Ozone Mapping and Profiler Suite (OMPS), and CALIOP data, the latter of which are generally used

to validate ALH datasets [16,17,25,26]. On the other hand, by utilizing OMI instruments sensitive to aerosol absorption signals, Satheesh et al. [18] and Eswaran et al. [19] investigated the retrieval of improved OMI SSA data with synergistic use of MODIS AOD data. However, it was difficult to extrapolate accurately from 550 to 380 nm using MODIS AOD data.

'Best' AOD datasets may be produced by merging individual AOD products. Levy et al. [20] merged MODIS dark target (DT) and deep blue (DB) products based on the normalized difference vegetation index (NDVI) to provide AOD products with larger spatial coverage than individual products. Xue et al. [21] provided merged AOD products of MODIS DT, DB, MISR AOD, and Sea-Viewing Wide-Field-of-View Sensor (SeaWiFS) AOD data using the optimal interpolation (OI) technique. Tang et al. [22] produced an AOD fusion dataset using the Bayesian Maximum Entropy (BME) method. Neither of these studies considered pixel-level AOD uncertainty. However, Xu et al. [23] applied the maximum likelihood estimation (MLE) method in assessing uncertainty, calculating the root mean square error (RMSE) values for AOD and surface reflectance data, and using it as a weighting factor for individual AOD products. Xie et al. [24] corrected the systematic bias in the method of Xu et al. [23], successfully merging Advanced Along-Track Scanning Radiometer (AATSR) data with three algorithms.

The AMI aboard the Geostationary Korea Multi-Purpose Satellite 2A (GEO-KOMPSAT-2A) was launched in December 2018 by the Korea Meteorological Administration (KMA) and Korea Aerospace Research Institute (KARI). The Geostationary Ocean Color Imager-2 (GOCI-2) and GEMS Geostationary Korea Multi-Purpose Satellite 2B (GEO-KOMPSAT-2B) satellites were launched in February 2020 [6,27]. These three payloads (AMI, GEMS, and GOCI-2) provide hourly aerosol data during daytime over East Asia including China and Japan, where the highest AOD values with highly variable compositions are observed. However, the three aerosol products have different characteristics, owing to variations in instrument specifications and aerosol algorithms, with no single aerosol product being superior to the others under specific conditions. The AMI, GEMS, and GOCI-2 instrument specifications are listed in Table 1, together with the advantages and disadvantages in aerosol data retrieval for each instrument.

AMI IR channels have a high spatial resolution of 2 km and are thus beneficial for cloud detection, including cirrus clouds. The higher spatial resolution of visible channels in both AMI (0.5–1 km) and GOCI-2 (0.25 km) than in GEMS (3.5 × 8 km at Seoul) are beneficial for detecting small-scale cloud contamination [28]. Visible and near-IR (NIR) channels in both AMI and GOCI-2 are also sensitive to aerosol size, whereas GEMS has no visible channels beyond 500 nm, and coarser spatial resolution than those of AMI and GOCI-2. GEMS is therefore less sensitive to aerosol size signals with its limited spectral range (300–500 nm). It is also difficult for GEMS to distinguish sub-pixel cloud contamination signals from top-of-atmosphere (TOA) reflectance because of its relatively large pixel size. However, GEMS has UV channels that are beneficial for detecting aerosol absorption and height signals because of the stronger Rayleigh signal than that of visible channels. GEMS UV channels also enable retrieval of aerosol properties over bright surfaces (usually source regions) more accurately due to dark UV surface reflectance.

Choi et al. [29] demonstrated aerosol retrieval results using Geostationary Ocean Color Imager (GOCI) data and validated GOCI AOD, Ångström exponent (AE), FMF, and SSA products over land and ocean sites. The GOCI Yonsei aerosol retrieval (YAER) AOD data were highly correlated with data-point fractions within the expected error ranges of MODIS DT [30] of 60% and 71% for land and ocean, respectively. Although GOCI FMF and AE data are less accurate than AOD data, they are still useful qualitatively [29,31]. Lim et al. [9] retrieved AOD, AE using AHI data, a geostationary meteorological imager (MI), and validated results over land and ocean sites. Regardless of the surface reflectance calculation method (minimum reflectivity (MRM) or estimated surface reflectance (ESR) method), AOD accuracy was better over ocean than land, owing to lower oceanic surface noise levels. As GOCI and AHI use visible and IR channels, AE and FMF data may be used qualitatively to infer particle-size information. However, SSA from GOCI, and AHI data are relatively inaccurate compared with SSA values calculated using the UV–visible aerosol algorithm [32,33].

Table 1. Specifications of Advanced Meteorological Imager (AMI), Geostationary Environment Monitoring Satellite (GEMS), and Geostationary Ocean Color Imager-2 (GOCI-2) instruments.

	GEO-KOMPSAT-2A	GEO-KOMPSAT-2B	
Payload	**AMI**	**GEMS**	**GOCI-2**
Number of Channels (μm)	16 (0.47–13.31)	1000 (0.3–0.5)	12 + 1 wideband (0.38–0.865)
Temporal resolution	within 10 min full disk (FD)	1 h (8 times per day)	1 h (10 times per day (local) + 1 time (FD))
Spatial resolution	1 km (<0.865 μm, Visible) 0.5 km (=0.64 μm, Visible) 2 km (>1.38 μm IR)	Gas: 7(NS) × 8(EW) km^2 Aerosol: 3.5(NS) × 8(EW) km^2	250 m at 130°E 1 km (FD)
Spectral resolution	37–125 nm (<1.6 μm) 475–1038 nm (IR)	<0.6 nm (3 samples) (sampling < 0.2 nm)	10–40 nm, 500 nm
Field of regard (FOR)	FD	5000 km (N/S) × 5000 km (E/W) N/S: 45°N–5°S E/W: 75°E–145°E (E/W, selectable)	2500 km (N/S) × 2500 km (E/W) FD (once per day)
Baseline products	Surface Analysis Cloud, Precipitation Aerosol, Radiation (AOD, Asian dust detection, particle size) Atmospheric condition, Aviation	O_3 (column, profile) NO_2, SO_2, HCHO, Aerosol (AOD, UVAI, SSA, ALH), UVI, CHOCHO, SFC, CLD	Water quality variable Marine environmental products Atmospheric properties: AOD, dust detection, aerosol type Land variable
Advantages for aerosol retrieval	Cirrus cloud detection High spatial resolution (500 m–2 km) Sensitive to aerosol size	Sensitive to aerosol absorption and height information Aerosol retrieval over relative brighter surface (e.g., city, desert)	High spatial resolution (250 m) Sensitive to aerosol size
Disadvantages (limitations) for aerosol retrieval	Difficult to retrieve aerosol of brighter surfaces over land (e.g., city, desert) due to high surface reflectance in visible channel.	Cirrus, sub-pixel cloud contamination Insensitive to aerosol size	Cirrus cloud contamination

In this study, we investigated the possibility of constructing an optimal aerosol dataset by synergistic use of GEMS, hyperspectral UV–visible, and AMI broadband MI data. As GEMS data are not yet released, LEO satellite OMI and MODIS instruments were used to provide proxy datasets for GEMS and AMI, respectively. Both GEMS and OMI are grating imaging spectrometers, providing hyperspectral data for wavelengths of 300–500 nm with full-width at half-maximum (FWHM) values of ~0.6 nm and spectral sampling of 0.2 nm. The main differences between GEMS and OMI data are the spatial resolution (3.5 × 8 and 13 × 24 km, respectively) and temporal resolution (eight times and once per day, respectively). MODIS has all wavelengths corresponding to the AMI visible–thermal IR range (470 nm, 511 nm, 640 nm, 856 nm, 1.38 μm, 1.61 μm, 6.952 μm, 8.562 μm, 11.212 μm, and 12.364 μm) needed for this study. The AMI and MODIS systems differ in terms of spatial resolution for each wavelength, being respectively 1 km and 500 m at 470 nm; 1 km and 1 km at 511 nm; 500 m and 250 m at 640 nm; 1 km and 250 m at 856 nm; 2 km and 1 km at 1.38 μm; 2 km and 500 m at 1.61 μm; 2 km and 1 km at 6.952 μm, 8.562 μm, 11.212 μm, and 12.364 μm. The systems also differ in terms of temporal resolution, with AMI once per 10 min and MODIS once per day. The overall procedure in constructing optimal aerosol datasets involved three stages: (1) improvement of GEMS cloud mask results with MI; (2) refining of GEMS predominant aerosol size mode selection among absorbing fine pollution particles (BC) and dust (DS) using broadband MI; (3) merging of the individual Level 2 (L2) AOD products and improved GEMS and MI products to create 'best' AOD datasets. Baseline GEMS aerosol products include AOD, SSA, and ALH products. The AOD and SSA products were compared using Aerosol Robotic Network (AERONET) data, and ALH and CALIOP datasets were compared by calculating ALH from backscattered coefficient data at 1064 nm.

OMI and MODIS data are described in Section 2; algorithms for synergistic use of the broadband MI are described in Section 3; results of synergistic use of the MI in terms of cloud masking and aerosol-type selection are described with aerosol product fusion results in Section 4; error analyses

before and after synergistic use of MI are investigated in Section 5. Sections 6 and 7 summarizes the results with future perspectives.

2. Data Description

2.1. OMI

OMI [34,35] is a grating imaging spectrometer of the push-broom type that simultaneously measures solar radiation backscattered from Earth at 270–500 nm with 0.6 nm spectral resolution using a two-dimensional charge-coupled device (CCD) of 580 spatial pixels × 780 spectral pixels. The instrument has the purpose of retrieving concentrations of atmospheric trace gases such as O_3, NO_2, SO_2, HCHO, and aerosols. Spatial resolution at nadir is ~13 km (along-track) × 24 km (across-track). The OMI instrument is aboard the Aura satellite, in the A-train satellite constellation. Aura was launched in July 2004, and the OMI has since provided data continuously. The satellite covers the globe once per day, and provides data every two days because of the 'row anomaly' problem that has existed since 2007 [36]. The row anomaly corresponds to a row on the CCD detector with poor-quality Level 1B (L1B) radiance data at all wavelengths that correspond to a particular viewing direction of the OMI.

OMI L1B version 3 radiance data produced by a visible detector (OML1BRVG) at wavelengths of 349–504 nm were used in this study, and OMI L1B version 3 visible irradiance data (OML1BIRR) were used to calculate normalized radiance. Apart from the row-anomaly CCD pixels, OMI radiances are known to degrade by 1–2%, and irradiances by 3–8%, over the mission lifetime of ~12 years [36]. The GEMS aerosol retrieval algorithms [33,37] were adopted for OMI L1B data to retrieve AOD and SSA data at 443 nm and ALH from 1 January to 31 December 2006. The spatial domain was East Asia (110°E–150°E; 20°N–50°N).

2.2. MODIS

2.2.1. MODIS L1B Data

MODIS aboard the Aqua satellite is used to take advantage of the continuous eight-minute time difference from OMI. The Aqua satellite was launched by the National Aeronautics and Space Administration (NASA) in 2002 and passes from south to north over the equator in the afternoon (1:30 p.m. local time). The ground swath of MODIS/Aqua is 2330 km (across-track), covering the entire Earth surface every two days and acquiring data in 36 spectral bands from visible to IR with a spatial resolution of 250 m for bands 1–2, 500 m for bands 3–7, and 1000 m for bands 8–36.

Here, Aqua MODIS L1B Collection 6 (C6) [38] data were used to generate the total dust confidence index (TDCI) [39] from MODIS IR data from 1 January 1 to 31 December 2006, for the above spatial domain. Calibration for MODIS L1B C6 was improved compared with MODIS L1B Collection 5 (C5) data, and a number of aerosol algorithm improvements have been published [40,41] (Section 3.2).

Although the TDCI can be retrieved from MODIS aboard Terra, we used only that aboard Aqua. The goal of this study was to investigate the possibility of synergy between GEMS and AMI data, with the time difference between the two being <10 min. Terra crosses the equator at 10:30 a.m. local time, so there is a three-hour time difference from the Aqua MODIS system. Terra TDCI data may thus not apply due to aerosol transport within the three hours, hence the use of Aqua data only.

2.2.2. MODIS Dark Target Aerosol Products

MODIS DT aerosol algorithms have been developed for dark surfaces (e.g., clear ocean surfaces and dense vegetation over land) [20,42]. The algorithms retrieve AOD parameters based on the assumption that for the two visible channels of 470 and 644 nm, surface reflectance can be estimated linearly from that of the shortwave IR channel at 2119 nm, which is transparent for aerosol signals. MODIS DT collection 6.1 (C6.1) was recently updated with surface reflectance data over land where urban coverage is >20% [43].

Here we used the MODIS aerosol product (MYD04) L2 C6.1, which has a spatial resolution of 10 × 10 km. Specifically, 'Optical_Depth_Land_And_Ocean' was applied, providing AOD at 550 nm for both ocean (quality flag = 1, 2, 3) and land (quality flag = 3).

MODIS DT aerosol products were used to create 'best' AOD data as proxy data for AMI aerosol products. Other MODIS aerosol algorithms (e.g., DB and MODIS Multi-Angle Implementation of Atmospheric Correction (MAIAC)) were not used because the MODIS DT aerosol algorithm uses only wavelengths of >470 nm. With wavelengths of >470 nm it is difficult to retrieve accurate AOD data for bright surfaces over land such as deserts and cities, because surface reflectance contributions are larger than the TOA aerosol contribution; the same properties can be observed in AMI aerosol products.

2.2.3. MODIS Black Sky Albedo

In the merging of individual AOD products to create the 'best' AOD datasets, the accuracies of the original satellite AOD products were assessed with respect to the corresponding surface albedo. MODIS black sky albedo (*BSA*) visible (0.3–0.7 μm) products (MCD43A3 version 6) were used as surface albedo in the absence of diffuse radiation, providing data daily at 0.5 km (~0.005°) spatial resolution. The *BSA* was derived by integrating the bidirectional reflectance distribution function (BRDF) for the upper hemisphere with respect to reflected angle [44]. MODIS BRDF products are retrieved using multidate, multiband, atmospherically corrected surface-reflectance data from the Aqua and Terra MODIS systems with a 16-day cycle. *BSA* can be expressed as follows:

$$BSA(\omega_i) = \int^{2\pi} BRDF(\omega_r,\ \omega_i)\cos(\theta_r)d\omega_r = \int^{2\pi} \frac{dI(\omega_r)\cos(\theta_r)d\omega_r}{I(\omega_i)\cos(\theta_i)d\omega_i} \quad (1)$$

where $dI(\omega_r)$ is the portion of total radiance reflected in the direction defined by ω_r, θ_r is the angle between the normal to the surface and the direction of reflected light, $d\omega_r$ is the element of the solid angle, $I(\omega_i)$ is the radiance incident on the surface from the direction ω_i, and θ_i is the angle between the normal to the surface and the direction of incident light. The accuracy of MCD43 in clear-sky situations is within 5%, as described by the MODIS land validation team [45]. Here, *BSA* was selected for a given day, with all quality data being used.

2.3. CALIOP

CALIOP aboard the Cloud-Aerosol Lidar and Infrared Pathfinder Satellite Observation (CALIPSO) satellite was launched on 28 April 2006, and is an LEO active lidar instrument that passes over the equator from south to north at 1:30 p.m. local time in the A-train constellation. CALIOP utilizes three receiver channels: one measuring 1064 nm backscatter intensity, and two measuring orthogonally polarized components of the 532 nm backscattered signal. From these three receiver channels, high-resolution vertical aerosol and cloud profiles for up to 40 km above sea level have been provided since mid-June 2006 during both day- and night-time. Although the horizontal spatial resolution of CALIOP is high at 333 m [46], because of the consistent short time gap between CALIOP and MODIS (<~2 min) or OMI (<~8 min during 2005 to 2007), it provides useful synchronous data for altitudes of clouds and aerosols, which cannot be probed by nadir viewing satellites [13]. CALIOP provides clear-sky, cloud, tropospheric aerosol, and stratospheric aerosol data separately through the 'vertical feature mask' variable, as well as high-resolution vertical profiles of aerosol and cloud.

In this study, the most recent version 4.2.0 standard product (CAL_LID_L2_05kmAPro-Standard-V4-20) was adopted to calculate ALH from 1064 nm total-attenuated-backscatter (km^{-1} sr^{-1}) daytime measurement data. Although CALIOP provides both 532 and 1064 nm non-polarized backscatter attenuation data, the 532 nm data appear to lose sensitivity in the presence of carbonaceous aerosols due to attenuation [13], so 1064 nm data were used. ALH values calculated from CALIOP

data were used in GEMS ALH validation. ALH (Z_{aer}) is defined as the attenuated-backscatter-weight height [13,47], expressed as:

$$Z_{aer} = \sum_{i-1}^{n} H(i)\left[\frac{B_{sc}(i)}{\sum_{i=1}^{n} B_{sc}(i)}\right] \quad (2)$$

where n represents the layer number from the surface to 10 km altitude, and $B_{sc}(i)$ represents the attenuated backscatter at height $H(i)$. A Gaussian shape with 1 km FWHM was assumed for the aerosol vertical distribution. This ALH concept was first introduced to the Total Ozone Mapping Spectrometer (TOMS) near-UV aerosol algorithm and was also used in the OMI aerosol algorithm [13,47]. Torres et al. [47] investigated the sensitivity of TOMS retrieved SSA and AOD data to aerosol vertical distribution using the Micropulse Lidar data of the South African Regional Science Initiative (SAFARI 2000) campaign [48]. The Gaussian shape implies that ALH has no significant effect on AOD (2–13%) and SSA (~0.1%) retrieval results, except for days with two aerosol layers [47].

2.4. AERONET

AERONET is a global aerosol monitoring network involving ground-based sun–sky photometer [49]. Sun–sky photometers measure direct sun irradiance and directional sky radiance in almucantars [50]. The direct sun data provide column-integrated AOD at nominal standard wavelengths of 340, 380, 440, 500, 675, 870, 935, 1020, and 1640 nm, and have been used for ground-truth AOD measurements for over 25 years. Column-averaged aerosol microphysical and optical properties (e.g., refractive index, volume size distribution (VSD), and SSA) at 440, 670, 870, and 1020 nm are retrieved by combining the AOD data and almucantar sky measurements at the four wavelengths.

Uncertainties in AERONET direct-measurement AOD data range from ±0.01 at visible wavelengths to ±0.02 at near-UV wavelengths [51]. For AERONET version 2 L2 inversion data, the theoretical uncertainty of SSA data is ±0.03 for 440 nm AOD > 0.4 [51,52]. AERONET inversion SSA data are provided only for 440 nm AOD > 0.4, so SSA data can be compared only under those conditions. Uncertainties in SSA are caused mainly by instrument calibration inaccuracies [52]. The instruments are calibrated regularly with reference Cimel instruments at the NASA Goddard Space Flight Center, using the Langley method. The AERONET database has been updated recently to version 3 [50], with the new algorithm providing cloud screening and automatic instrument anomaly control. The AERONET version 3 L2 database also allows more AOD observations under partly cloudy conditions [53]. Reported AERONET AOD differences between versions 3 and 2 average +0.002 (±0.004 standard deviation, SD) for time-matched observations [50].

Here, AERONET L2 AOD values at 380 and 440 nm, and SSA values at 440 nm, were used to compare satellite-retrieval AOD and SSA data. AERONET direct-measurement AOD data were used as true references for validation of satellite-retrieval AOD data, while the comparison of satellite-retrieval SSA and AERONET SSA data are not considered appropriate for validation because both inversion techniques involve assumptions [32]. In field studies [54,55], Jethva et al. [32] found that although the theoretical uncertainty of AERONET SSA is ±0.03, the actual uncertainty may be ~±0.05. We, therefore, used both ±0.03 and ±0.05 uncertainty thresholds in comparisons of retrieved SSA and AERONET data.

3. Algorithm for Synergistic Broadband Meteorological Imager Use

Flowcharts for producing an optimal aerosol dataset are shown in Figures 1 and 2, with the former pertaining to the improvement of GEMS aerosol algorithms in terms of cloud masking and predominant aerosol size mode selection, and the latter to the merging of the improved GEMS and MI aerosol products.

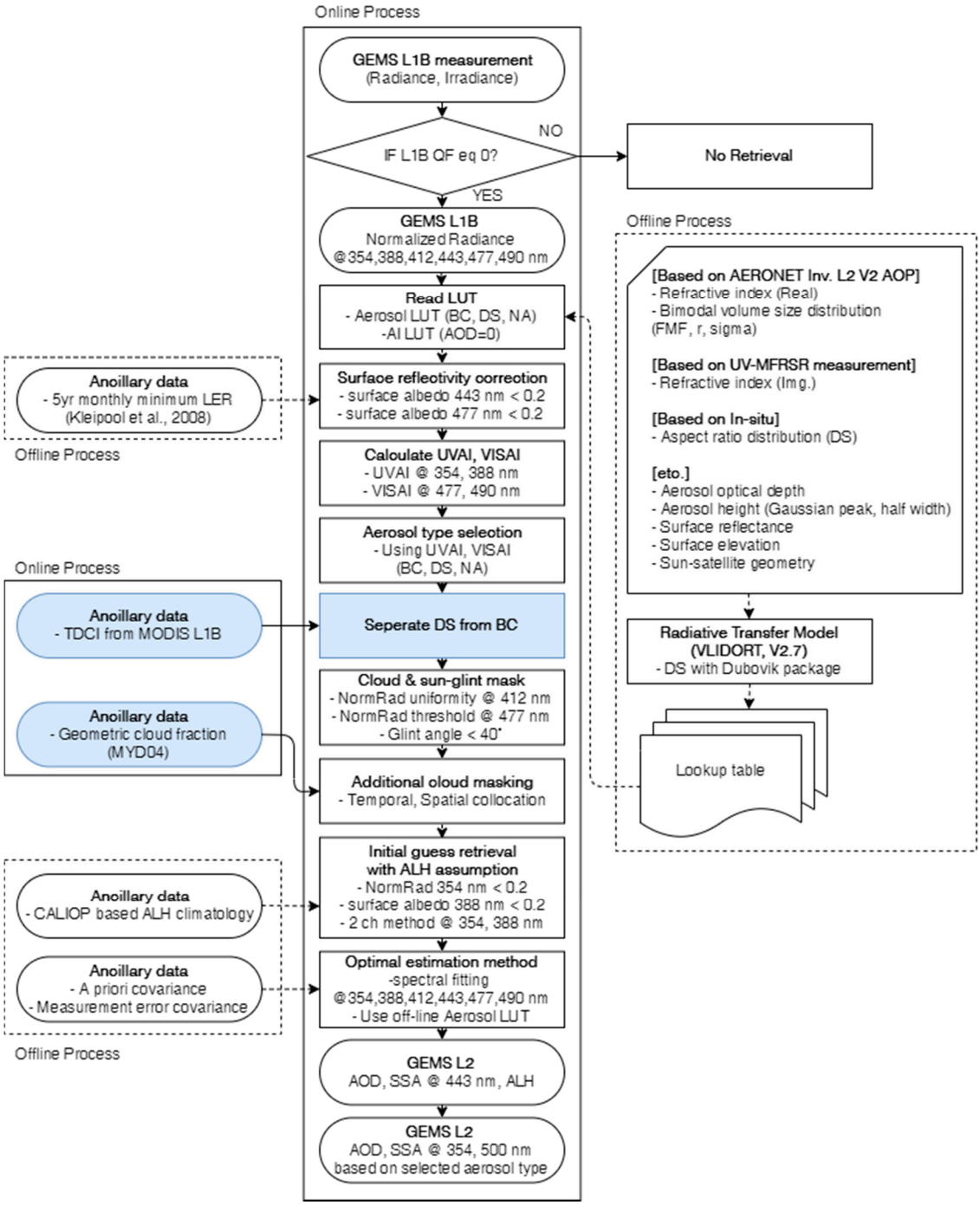

Figure 1. Flowchart describing synergistic use of meteorological imager for GEMS aerosol algorithm improvement. The unshaded components correspond to the GEMS aerosol algorithm [33,37]. The figure is modified from Figure 1 of Go et al. [33]. Blue shading indicates synergistic use of meteorological instruments.

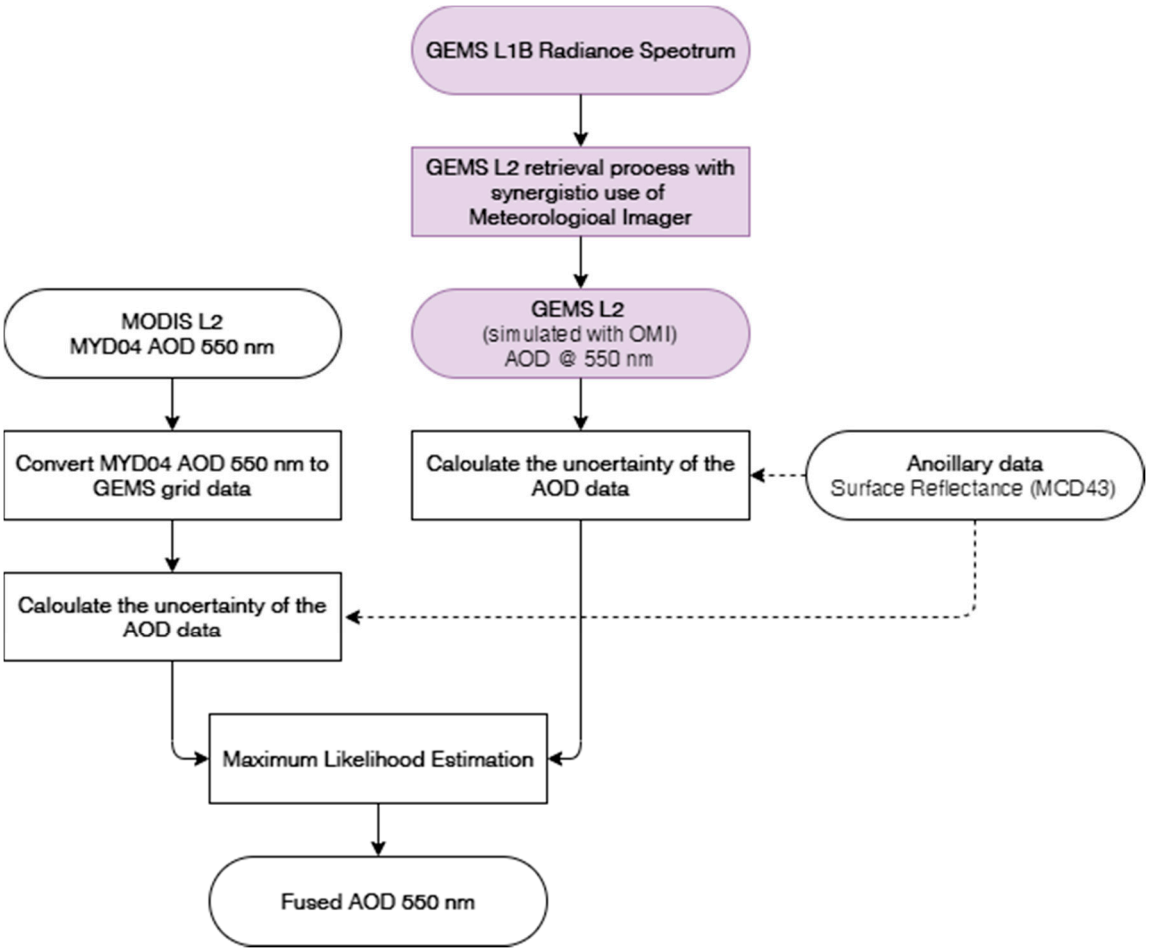

Figure 2. Flowchart describing synergistic use of meteorological instruments to create 'best' aerosol optical depth (AOD) datasets by merging individual AOD products. Purple-shaded components correspond to Figure 1.

The unshaded components of Figure 1 correspond to the GEMS aerosol algorithm, which was developed and tested continuously with OMI L1B data; improvements have been described in previous studies [33,37]. The blue shading indicates synergistic use of a meteorological instrument, with MI cloud masking (Section 3.1) being applied first. The high spatial resolution of the MI with IR channels helped mask sub-pixel clouds and cirrus clouds for GEMS aerosol retrieval results. The TDCI, calculated from MI IR channels, was applied next to the GEMS aerosol algorithm to separate dust from the GEMS aerosol type. Corrected aerosol types were applied to the GEMS aerosol algorithm (Section 3.2). Finally, as shown in Figure 2, GEMS and MI AOD data were combined using the MLE method by applying weights calculated from the RMSE of the original AOD products (Section 3.3). Detailed descriptions of each step are provided below.

3.1. GEMS Aerosol Algorithm and Synergistic Use of Cloud Masking

Detailed descriptions of improvements to the GEMS aerosol algorithm have been published previously [33,37]. GEMS aerosol algorithms are based on optimal estimation (OE) involving an off-line look-up table (LUT). Aerosol models included in the LUT were integrated from the long-term AERONET inversion dataset. The spectral dependence of aerosol absorption at wavelengths of <440 nm was refined using UV Multi-Filter Rotating Shadowband Radiometer (UV-MFRSR) ground-based measurement data obtained over Seoul, Korea, to give the most appropriate spectral aerosol absorption model for East Asia [49,56]. The Dubovik package [57–59] was applied to generate the LUT for the DS aerosol model. The aspect ratio distribution of DS was adopted from previous field data [60–63],

because of the aspect ratio distribution varying by region [58]. For the inversion procedure, the aerosol types BC, DS, and non-absorbing (NA) were first selected by calculating UVAI and visible aerosol index (VISAI) values. Surface reflectance corrections were based on the minimum Lambertian equivalent reflectivity (LER) [64]. Initial AOD and SSA estimates were retrieved using a two-channel method, and ALH was retrieved using an OE method involving six channels (354, 388, 412, 443, 477, and 490 nm). The definition of ALH in this study was defined in Equation (2).

MODIS L2 provides cloud-mask products, which were applied in the aerosol retrieval algorithm at a 500-m spatial resolution, with 0 indicating clear conditions and 1 cloudy conditions. For each pixel of MODIS L2, the nearest GEMS pixel was allocated, and MODIS L2 pixels within a GEMS pixel were averaged. If the average cloud fraction for a GEMS pixel was above a certain value (from 20% to 80%), that pixel was considered contaminated by cloud, and masked.

3.2. Total Dust Confidence Index

The 300–500 nm channels cannot distinguish easily between smoke and dust, with both types of particles causing Mie scattering in that range. Mie scattering efficiency is at the maximum when particle diameter and wavelength are similar. Particle size does not distinguish easily between smoke and dust in the 300–500 nm range. However, IR channels can distinguish between smoke and dust, with smoke involving Rayleigh scattering and dust Mie scattering. Previous studies have demonstrated dust particle detection using IR channels such as 8.6, 11, and 12 μm. Park et al. [39] developed a new dust detection algorithm involving the TDCI, overcoming previous dust-detection limitations in distinguishing clear-sky pixels, optical properties of dust particles, and cloud contamination.

The TDCI algorithm uses 6.3, 8.6, 11, and 12 μm wavelengths, which are applicable for both MODIS and AMI instruments, with TDCI > 40 indicating a dust aerosol type [39]. TDCI values are more accurate with high AOD and low FMF values [39]. For cases with TDCI > 40, FMF is <0.4 and AOD > 0.4, with agreement of TDCI being ~0.146 and for false detection 0.444 [39]. However, for cases with TDCI > 40, FMF < 0.4, and AOD > 1.0, the agreement of TDCI was 0.764 and 0.379 for false detection [39].

3.3. Maximum Likelihood Estimation Method

The MLE method provides a weighted average of original data products with statistical variables such as mean, number of counts, and SD being used as weighting factors. The method may consider pixel-level uncertainties of aerosol products. In this study, Equations (3) and (4) of the MLE method [23] were used to calculate merged AOD products at each point with merged AOD re-gridded from the original AOD value:

$$\tau_i^{MLE} = \sum_{k=1}^{N} \frac{\left(R_{i,k}\right)^{-2}}{\sum_{k=1}^{N}\left(R_{i,k}\right)^{-2}} \tau_{i,k} \tag{3}$$

$$R_{i,k} = \sqrt{\frac{\sum_{i=1}^{M}\left(s_{i,k} - g_i\right)^2}{M}} \tag{4}$$

where τ_i^{MLE} is the final AOD at the new spatial resolution of grid point i; $R_{i,k}$ is the SD of the new grid point i for the original AOD product k (SD can be used as a measure of AOD uncertainty for each AOD and surface albedo interval, and AOD expected error when no information is available for the true reference dataset, such as AERONET data); $\tau_{i,k}$ is the mean AOD value at the new spatial resolution of grid point i (from the spatial resolution of instrument-AOD original product k); N is the total number of original AOD products; $s_{i,k}$ is the mean instrument AOD at the new spatial resolution grid point i; g_i is the mean AERONET AOD value for gridded point i; M is the number of collocated points between $s_{i,k}$ and g_i. The term $s_{i,k}$ is the spatial average over 0.4°, and g_i is the temporal average over 30 min.

GEMS 443 nm AOD values simulated with OMI L1B data (Figure 2) were converted to 550 nm AOD values using the assumed absorption Ångström exponent (AAE) value. The MYD04 550 nm

AOD data were converted to GEMS grid data. Each MYD04 pixel was assigned to the nearest GEMS pixel and the collected MODIS data within each GEMS pixel were averaged. The RMSE values of each original instrument AOD product (MYD04 AOD and GEMS L2 AOD) were calculated. To merge several instrument's aerosol products without using ground-based measurement data such as AERONET, it was necessary to find the relationship of RMSE with other parameters concerning regional or global AOD products. Surface reflectance is a major source of AOD error. AOD magnitude is also a key parameter that affects AOD error; with strong AOD plumes, surface reflectance will not be the major source of error in AOD retrievals. Therefore, four sets of surface albedo values (0.0–0.05, 0.05–0.08, 0.08–0.11, and 0.11–0.25) and four sets of AOD values (0.0–0.25, 0.25–0.5, 0.5–0.8, and 0.8–5.0) were considered when calculating RMSE values [23]. For surface albedo, MODIS *BSA* visible (0.3–0.7 μm) products (MCD43A3 version 6) were used (MCD43 products are independent variables from the GEMS aerosol and MODIS DT aerosol products).

4. Results

4.1. Synergistic Use of Meteorological Imagers for Cloud Masking

Case-study results for synergistic use of an MI in cloud masking are shown in Figure 3. The IR channels detect cirrus clouds, owing to ice particle absorption properties. The GOCI red–green–blue (RGB) images for 22 May and 25 May 2016, are shown in Figure 3a,b, respectively, with each being a combined true-color TOA-reflectance image for 660 (red), 555 (green), and 490 nm (blue) after correction of the Rayleigh optical depth signal. On 22 May, cirrus clouds were present over the northeastern Korean Peninsula and Russia at 130°E–135°E, 45°N–50°N. The GEMS AOD results retrieved using OMI L1B data are shown in Figure 3c, with cirrus cloud regions being misidentified as high aerosol plumes with AOD values of >2.5. The MODIS and AHI cloud-mask data were used with the GEMS AOD algorithm to mask the misidentified pixels. Figure 3e,g show the effect of synergistic use of MODIS (500 m spatial resolution) and AHI cloud-mask data, respectively; in both cases, the cirrus clouds are well masked. In contrast, Figure 3b,d,f,h show thick aerosol plumes, including over the western Korean Peninsula and the ocean (Figure 3b,d). The aerosol plumes over the ocean remained after applying MODIS and AHI cloud masking as shown in Figure 3f,h, respectively.

Results of a GEMS 443 nm AOD validation test with OMI L1B data, 2005–2007, are shown in Figure 4, with AERONET L2 direct-sun AOD data being used as true references. Validation of GEMS AOD data constrained with MODIS cloud fractions of <80% to <20% (in sequential order) is demonstrated in Figure 4a–d.

Cloud generally has a higher optical depth than AOD, and most of the overestimated satellite-retrieval AOD points were caused by clouds. As the AOD-pixel cloud fraction decreased from Figure 4a–d, the overestimated pixels were screened out, especially over areas with AERONET AOD values of <1.0, with the correlation coefficient (R) increasing from 0.786 to 0.871, the RMSE decreasing from 0.341 to 0.276, and the Q (fraction of data points within the expected error range of 30% or 0.1; [65]) increasing from 46.77% to 57.32%. This demonstrates that MODIS cloud masking (i.e., high-spatial-resolution MI IR channel data) can be useful for improving GEMS AOD data in cases of cloud contamination.

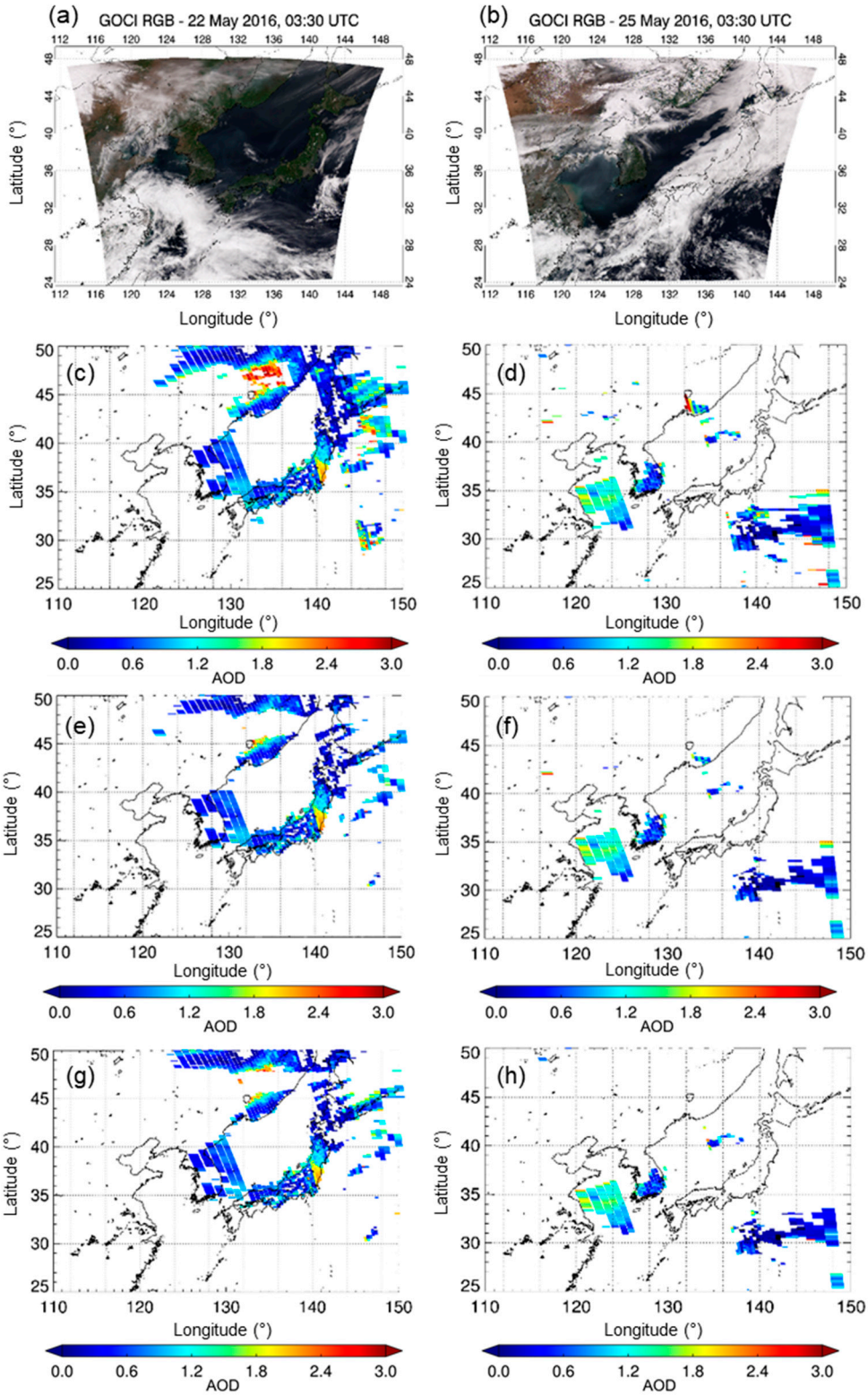

Figure 3. Case study of the synergistic use of meteorological imager (MI) for cloud masking on 22 May (**a**,**c**,**e**,**g**) and 25 May 2016 (**b**,**d**,**f**,**h**); with (**a**,**c**,**e**,**g**) representing cirrus cloud cases and (**b**,**d**,**f**,**h**) clear-sky cases. (**a**,**b**) represent the GOCI red–green–blue (RGB) image; (**c**,**d**) GEMS AOD retrieved with Ozone Monitoring Instrument (OMI) Level 1B (L1B) data; (**e**,**f**) retrieved GEMS AOD with synergistic use of Moderate-Resolution Imaging Spectroradiometer (MODIS) cloud-mask data (500 m); and (**g**,**h**) retrieved GEMS AOD with synergistic use of the Advanced Himawari Imager (AHI) cloud mask on 22 May and 25 May 2016, respectively.

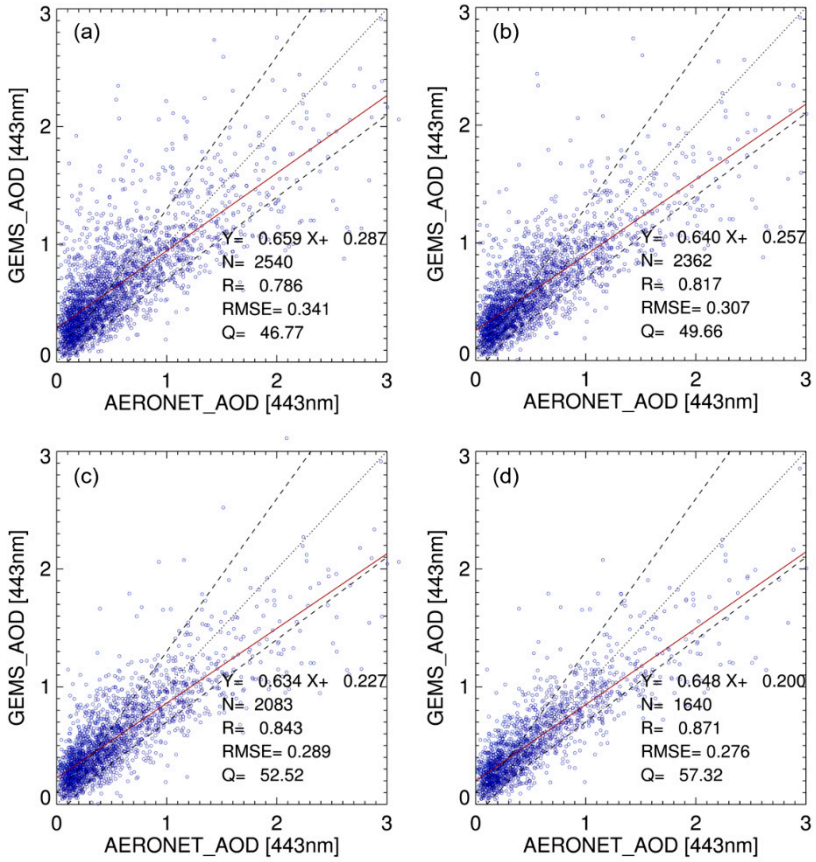

Figure 4. Validation of GEMS AOD with OMI L1B and Aerosol Robotic Network (AERONET) L2 direct-measurement data, 2005–2007, with MODIS cloud fractions of (**a**) <80%; (**b**) <60%; (**c**) <40%; (**d**) <20%. Dotted and dashed lines indicate 1:1 line and expected error of AOD (30% or 0.1; Ahn et al. [65]), respectively. Red line is the linear fitting line for validation results. Corresponding slope (A) and offset (B) for red line are presented in each figure in $y = Ax + B$ format.

4.2. Synergistic Use of Aerosol Type Selection

4.2.1. Application of TDCI

The application of TDCI to the GEMS aerosol retrieval procedure for a severe dust case (8 April 2006) is demonstrated in Figure 5 where (a) indicates MODIS RGB TOA reflectance data; (b) indicates GEMS aerosol types (BC, DS, NA) with UVAI and VISAI; (c) is the corresponding OMI UVAI; (d) shows the calculated MODIS TDCI as an indicator of dust (to clearly identify dust pixels, only TDCI values >40.0 are plotted); (e) shows GEMS aerosol types corrected from (b) after using TDCI; (f) shows a qualitative comparison of OMI aerosol types with OMI operational aerosol products. OMI operational aerosol products classify aerosol types as 'SMOKE', 'DUST', or 'SULFATE' based on UVAI and AIRS CO data [13]. The OMI aerosol types 'SMOKE', 'DUST', and 'SULFATE' in Figure 5f may correspond to 'BC', 'DS', and 'NA' aerosol types in GEMS (Figure 5b,e), respectively. On that particular day, high UVAI values with high TDCI (>40) were recorded for long, thick aerosol bands in the Manchuria region, with detection of coarse absorbing particles. The original GEMS aerosol type (Figure 5b) displayed most pixels as DS aerosols; however, after applying TDCI, this type remained only for severe aerosol plume areas. Conversely, the OMI aerosol type was 'SMOKE' in dust plume areas. Although OMAERUV applies a straightforward separation of the 'SMOKE' aerosol type based on AIRS CO data, dust aerosol can be classified as 'SMOKE' when present over a high-CO area such as eastern China during the spring season [13].

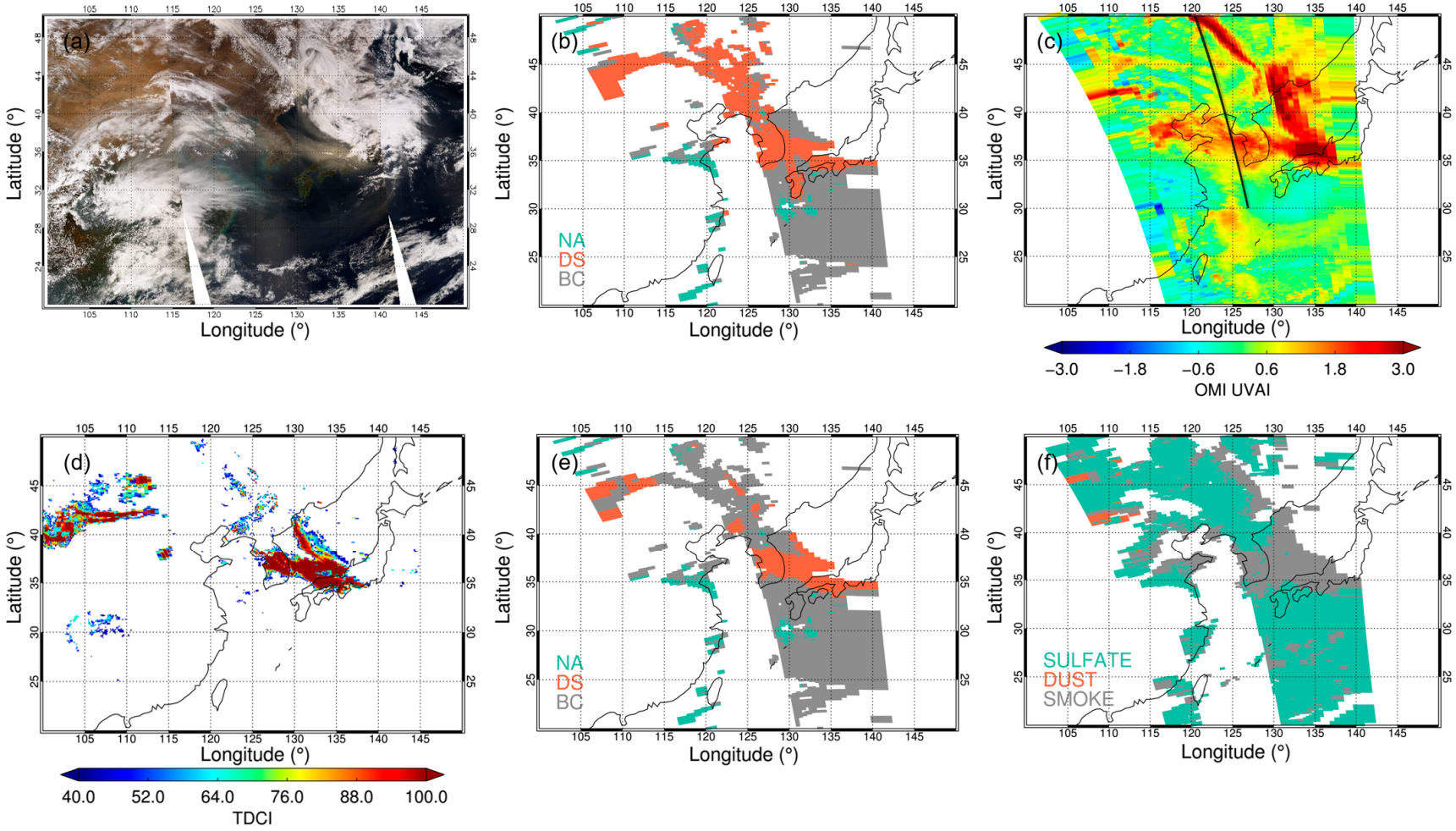

Figure 5. (**a**) MODIS RGB images for 8 April 2006, for the dust outbreak case; (**b**) GEMS aerosol type distinguished with ultraviolet (UV) aerosol index (UVAI) and visible aerosol index (VISAI) (fine pollution particles (BC), dust (DS), and non-absorbing (NA)); (**c**) OMI UVAI; (**d**) total dust confidence index (TDCI) calculated with MODIS; (**e**) GEMS aerosol type corrected with TDCI; (**f**) OMI aerosol type from operational (OMAERUV) products. OMI aerosol types 'SMOKE', 'DUST', and 'SULFATE' in (**f**) may correspond to 'BC', 'DS', and 'NA' aerosol types in GEMS (**b**,**e**), respectively.

Here, OMAERUV (Figure 5f) indicated much 'SULFATE' without appearing as NA in GEMS (Figure 5e) because of the different threshold for aerosol type selection. OMAERUV first applies UVAI to separate 'SMOKE' and 'DUST' (high UVAI) from 'SULFATE' (low UVAI), followed by AIRS CO data to separate 'SMOKE' (high CO) from 'DUST' (low CO). The GEMS aerosol algorithm first applies UVAI to separate BC and DS (high UVAI) from NA (low UVAI) types, followed by VISAI data to separate BC (low VISAI) and DS (high VISAI) types. Both the GEMS and OMI aerosol algorithm use UVAI, but our UVAI threshold was lower than that of OMI, causing detection of more BC aerosols. However, the BC-detection area in Figure 5e, over southern Japan, seems to have low RGB AOD values (Figure 5a), so the aerosol type has little practical meaning in this low-AOD case; rather, it is required only as a priori information for the aerosol retrieval procedure.

The MODIS RGB image for the same day (8 April 2006) is shown in Figure 6a, with Figure 6b,c showing the GEMS AOD and SSA data, respectively, before applying the TDCI-corrected aerosol type. Figure 6d displays TDCI calculated with MODIS; (e) and (f) represent GEMS AOD and SSA, respectively, after application of the TDCI-corrected aerosol type. The retrieved SSA value for the northern Korean Peninsula decreased from 0.96 to 0.92 (Figure 6c–f), whereas the retrieved AOD value (Figure 6b–e) for low-AOD dust-storm regions (105°E–130°E; 40°N–50°N) showed no significant change. Sensitivity tests of the GEMS aerosol algorithm (not shown here) indicate that when AOD is low, TOA reflectance does not change significantly with aerosol type. In contrast, for SSA, the lower the AOD, the lower its sensitivity to TOA reflectance, making it difficult to retrieve SSA accurately.

4.2.2. POCD and POFD Analysis

AERONET aerosol data were selected as reference data to validate aerosol types between forward and inverse models, based on GEMS (before and after applying the TDCI during the inversion procedure) and OMI aerosol types. Aerosol types were investigated qualitatively using AERONET data, applying traditional statistical analysis such as accuracy, probability of correct detection (POCD), and the probability of false detection (POFD) [66]. FMF and 440 nm SSA data were first used to classify aerosol type based on AERONET inversion L2 data [31] before Equations (5)–(7) for accuracy, POCD, and POFD were applied to compare the GEMS and AERONET aerosol types.

$$\text{Accuracy } (\%) = \frac{a+d}{a+b+c+d} \times 100 \tag{5}$$

$$\text{POCD } (\%) = \frac{a}{a+c} \times 100 \tag{6}$$

$$\text{POFD } (\%) = \frac{b}{a+b} \times 100 \tag{7}$$

Here a represents true detections (positives; i.e., the number of collocated points where both GEMS and AERONET algorithms indicate the existence of 'dust'); b represents false positives (i.e., the number of collocated points where AERONET indicates 'no dust' but GEMS indicates 'dust'); c represents false negatives (i.e., the number of collocated points where AERONET indicate 'dust' but GEMS indicates 'no dust'); d represents true negatives (i.e., the number of collocated points where both AERONET and GEMS algorithms indicate 'no dust').

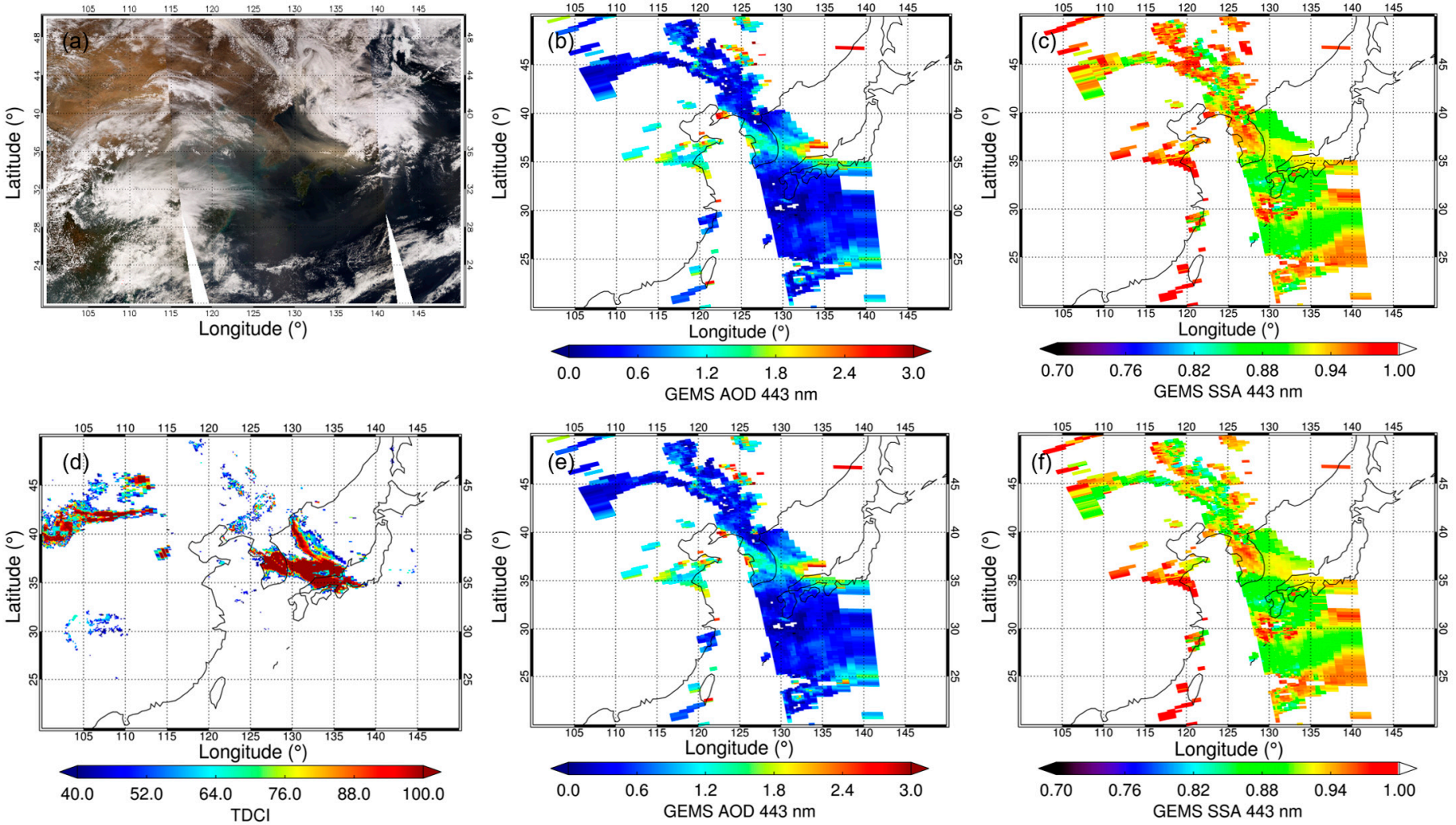

Figure 6. (**a**) MODIS RGB for 8 April 2006; (**b**) GEMS AOD before applying the TDCI-corrected aerosol type; (**c**) GEMS single-scattering albedo (SSA) before applying the TDCI-corrected aerosol type; (**d**) TDCI calculated with MODIS; (**e**) GEMS AOD after applying the TDCI-corrected aerosol type; (**f**) GEMS SSA after applying the TDCI-corrected aerosol type.

Calculated accuracy, POCD, and POFD results for 1 January to 31 December 2006, are shown in Tables 2–4, with statistics before and after applying the TDCI shown together for the GEMS aerosol type. For aerosol type BC, the GEMS POCD increased from 38% to 46% with the application of TDCI, while POFD increased from 16% to 47% and accuracy decreased from 62.5% to 52%. For the DS aerosol type, the GEMS the POCD decreased from 100% to 66%, while the POFD decreased from 93% to 82%. However, there were few DS *a* and *c* data points because of the use of AERONET inversion data points in the statistical analysis, so the POCD is not reliable. Nevertheless, the GEMS DS accuracy increased from 72% to 94% after applying the TDCI, due to the increased number of data points available for *d*. For the NA aerosol type, the number of data points for *a*, *b*, *c*, and *d* was the same before and after applying the TDCI. For the OMI aerosol type [13], the overall BC and DS accuracies were higher than that of the GEMS aerosol type. OMI uses AIRS CO data for separating the BC and DS aerosol types. The NA accuracy was lower than that of the GEMS aerosol type.

Table 2. Calculated accuracy, probability of correct detection (POCD), and probability of false detection (POFD) for BC detected GEMS aerosol type.

BC	**GEMS → GEMS + TDCI**			**OMI**		
AERONET (true reference)	A (31 → 38)		C (50 → 43)	A (15)		C (66)
	B (6 → 35)		D (74 → 45)	B (3)		D (77)
	Accuracy (62.5% → 52%)	POCD (38% → 46%)	POFD (16% → 47%)	Accuracy (57.14%)	POCD (18.52%)	POFD (16.67%)

Table 3. Calculated accuracy, POCD, and POFD for DS detected GEMS aerosol type.

DS	**GEMS → GEMS + TDCI**			**OMI**		
AERONET (true reference)	A (3 → 2)		C (0 → 1)	A (0)		C (3)
	B (44 → 9)		D (114 → 149)	B (1)		D (157)
	Accuracy (72% → 94%)	POCD (100% → 66%)	POFD (93% → 82%)	Accuracy (97.52%)	POCD (0%)	POFD (100%)

Table 4. Calculated accuracy, POCD, and POFD for NA detected GEMS aerosol type.

NA	**GEMS**			**OMI**		
AERONET (true reference)	A (9)		C (44)	A (35)		C (18)
	B (4)		D (104)	B (43)		D (65)
	Accuracy (70%)	POCD (16%)	POFD (30%)	Accuracy (62.11%)	POCD (66.04%)	POFD (55.13%)

For nadir-view instrument data, accurate aerosol-type retrieval is difficult because of its low information content. Although AERONET inversion data have high accuracy [51,52,58], the aerosol type-classification between forward (based on the method of Lee et al. [31]) and inverse modeling (based on UVAI, VISAI, and TDCI) are not identical. Therefore, the qualitative comparison method was used here to assess GEMS aerosol-type accuracy.

4.2.3. Validation of Aerosol Results after Applying TDCI

AOD validation and SSA comparison results before and after applying the TDCI are described in Figure 7, where (a), (c), and (e) represent AOD validation and SSA comparison results before applying TDCI; (b), (d), and (f) after applying TDCI. The GEMS 380 nm AOD values are extrapolated from 443 nm AOD data based on the AAE value of the selected aerosol type. SSA comparison results improved significantly after the application of the TDCI, but AOD validation showed no significant improvement. For SSA, the fraction of data points within the 0.03 difference range increased from 42% to 51%. The sensitivity test of the GEMS aerosol algorithm indicates that SSA is significantly affected by

incorrect aerosol size information, while AOD is less affected [37]. The 380 nm AOD validation results improved for high-AOD cases. The remaining error may thus be due to errors in surface reflectance data or forward aerosol modeling.

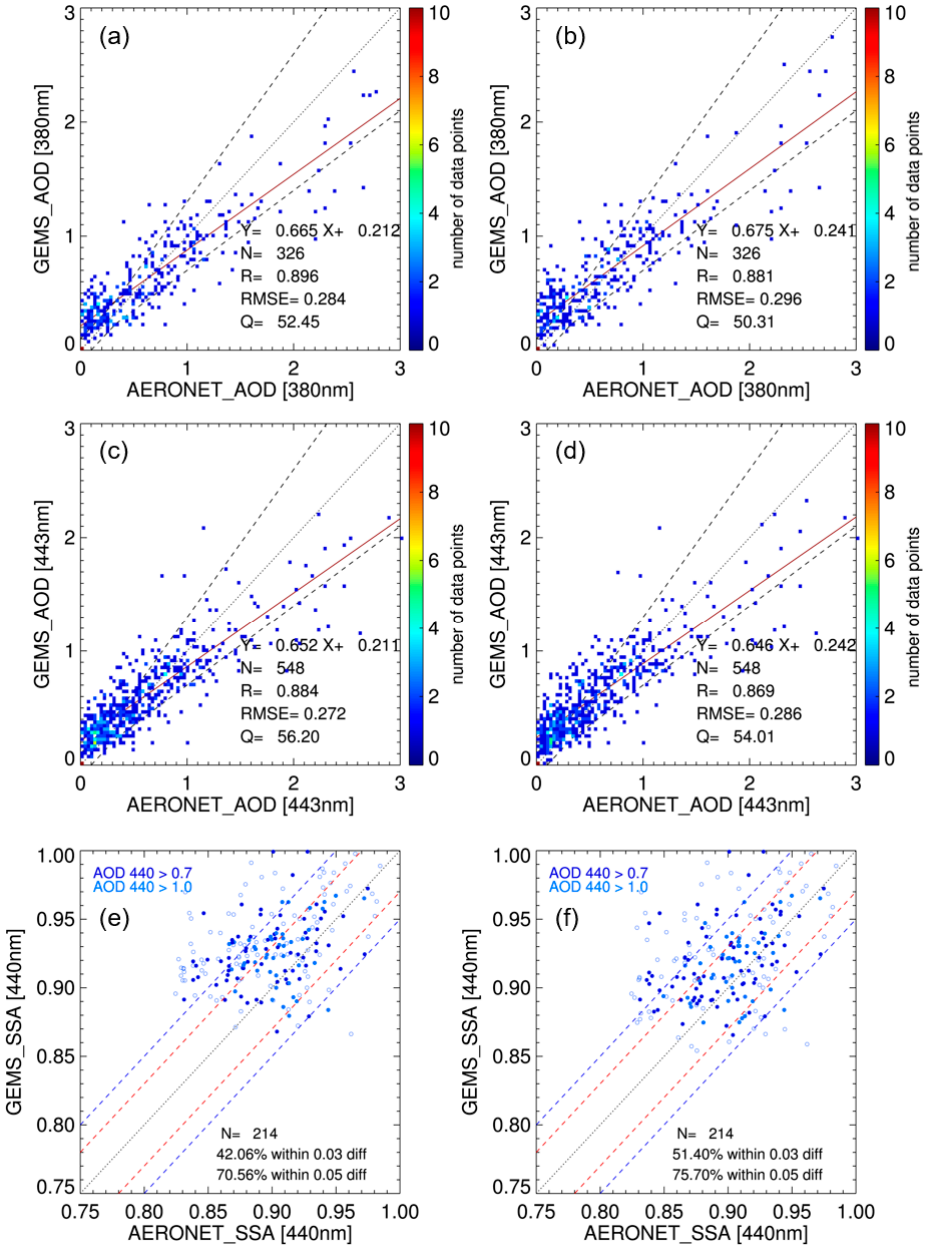

Figure 7. Validation results for GEMS AOD and comparison of GEMS SSA before (**a**,**c**,**e**) and after (**b**,**d**,**f**) applying TDCI. The 380 nm GEMS AOD values are extrapolated from 443 nm GEMS AOD with an absorption Ångström exponent (AAE) value of the selected aerosol type. In (**a**–**d**), dotted and dashed lines indicate 1:1 and expected error of AOD (30% or 0.1; Ahn et al. [65]) lines. The red solid line is the linear fitting line for AOD validation results. The corresponding slope (A) and offset (B) for the red line are presented in each figure in $y = Ax + B$ format. In (**e**,**f**), the dotted line is the 1:1 line. The red dashed line indicates the theoretical uncertainty ±0.03 of AERONET SSA at 440 nm [51]; the blue dashed line indicates ±0.05 uncertainty, which could be the actual error of AERONET SSA [32].

Results of bias analyses for retrieved ALH data are shown in Figure 8 before (a,c,e) and after (b,d,f) application of the TDCI. As mentioned in Section 2.3, the 1064 nm total attenuated backscatter (km^{-1} sr^{-1}) from version 4.2.0 Standard product (CAL_LID_L2_05kmAPro-Standard-V4-20) was used

to calculate CALIOP ALH. To exclude the presence of clouds and effects of noise, average attenuated backscattered (total 399 layers average) larger than 0.005, and smaller than 0.0015 were rejected, respectively [13]. CALIOP ALH were then calculated using Equation (2). GEMS ALH pixels within a 20 km radius of the CALIOP path were collected and used in the validation. Due to the lack of CALIOP data, the validation period was 13 June to 31 December 2006, with a total of 3064 data points. ALH bias (GEMS ALH minus CALIOP ALH) are listed sequentially in order of corresponding GEMS AOD, and 80 bins are collected into one. The circle and error bar in each bin represent the mean and SD of the 80 points collocated between GEMS aerosol and CALIOP data. Figure 8a,b indicate the ALH bias with respect to retrieved GEMS AOD values.

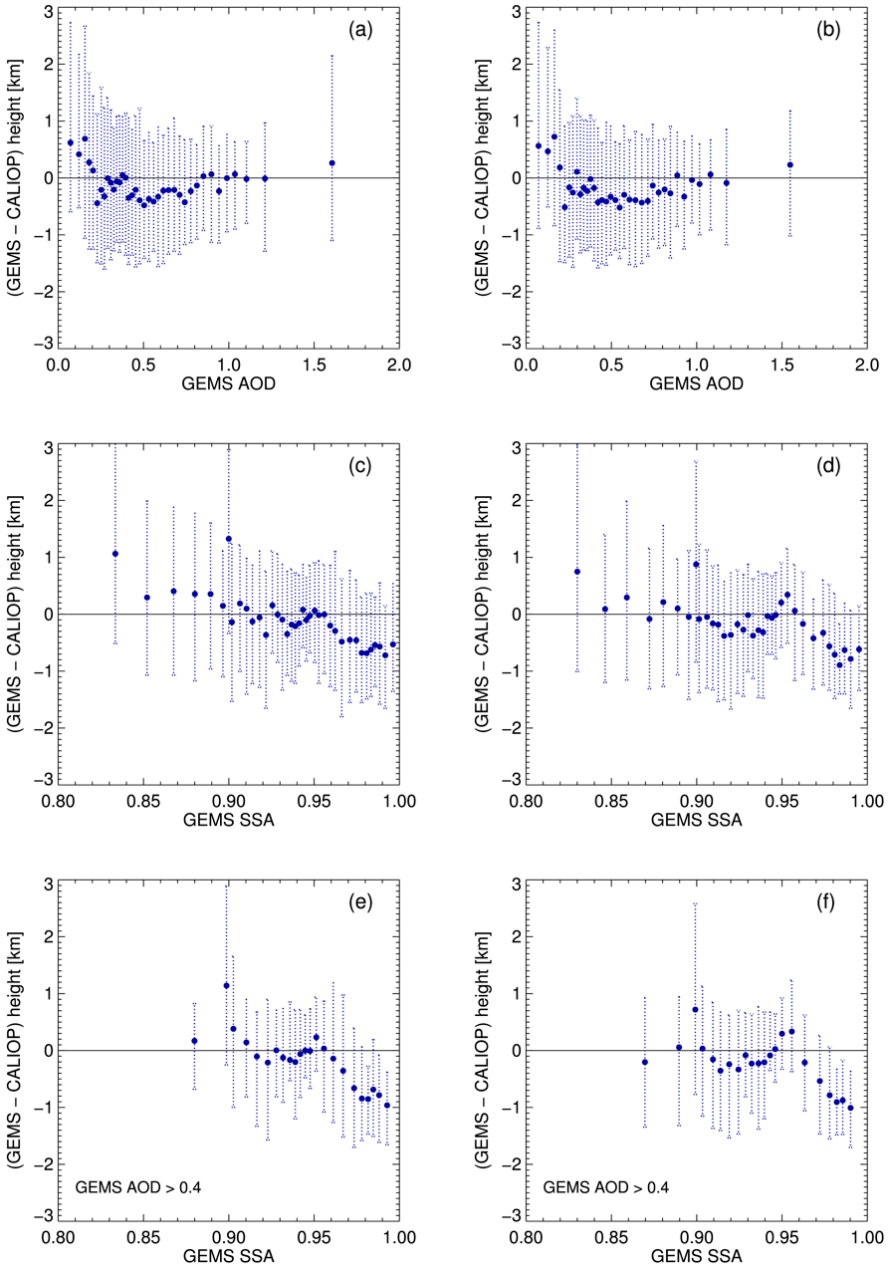

Figure 8. Aerosol layer height (ALH) bias before (**a**,**c**,**e**) and after (**b**,**d**,**f**) applying the TDCI value. (**a**,**b**) ALH bias with respect to retrieved AOD; (**c**,**d**) ALH bias with respect to retrieved SSA for all AOD; and (**e**,**f**) ALH bias with respect to retrieved SSA for AOD > 0.4. Circles and error bars represent mean and standard deviation (SD) for each bin of 80 collocated data points for GEMS aerosol and CALIOP data.

The overall mean ALH bias decreased slightly after application of the TDCI, with the bias approximating zero, especially for AOD > ~0.4. The ALH bias with respect to retrieved SSA for all AOD cases is indicated in Figure 8c and d. To clearly indicate ALH bias with respect to SSA only, GEMS AOD < 0.4 were omitted in Figure 8e,f. AERONET SSA is reported only for AOD > 0.4, because SSA sensitivity and accuracy are low when AOD is low [51,52]. Figure 8e,f indicate the ALH bias with respect to retrieved SSA for GEMS AOD > 0.4, with the bias being close to zero for both cases, especially with absorbing particles (SSA < 0.95). This is consistent with UV channels being more sensitive than visible channels to aerosol absorption signals due to the predominant Rayleigh scattering.

4.3. AOD Fusion Results

4.3.1. Weight Calculation

Calculated RMSE values for GEMS AOD simulated with OMI L1B data, and MODIS DT AOD data for the three years 2005–2007 are given in Table 5, which indicates that the RMSE values satisfactorily indicate characteristics of GEMS and MODIS AOD. For bright-surface albedo ranges of 0.08–0.11 and 0.11–0.25, the number of GEMS AOD data points (36, 5, and 13) and data number percentages (3.54%, 0.49%, and 1.28%; see Table caption for definition) were higher than those of MODIS DT AOD data.

Table 5. Calculated root mean square error (RMSE) of GEMS AOD simulated with OMI L1B data and MODIS dark target (DT) AOD. GEMS number and MODIS number indicate the total number of validation points, respectively. Data number (%) indicates the (GEMS number/Total GEMS number) × 100 and (MODIS number/Total MODIS number) × 100, respectively.

Black Sky Albedo	AOD	GEMS RMSE	GEMS Number	Data Number (%)	MODIS DT RMSE	MODIS Number	Data Number (%)
0.0–0.05	0.0–0.25	0.087	162	15.93	0.123	361	23.97
	0.25–0.5	0.154	232	22.81	0.129	326	21.65
	0.5–0.8	0.247	192	18.88	0.224	197	13.08
	0.8–5.0	0.509	101	9.93	0.300	188	12.48
0.05–0.08	0.0–0.25	0.117	55	5.41	0.142	125	8.3
	0.25–0.5	0.140	96	9.44	0.153	104	6.91
	0.5–0.8	0.212	56	5.51	0.250	65	4.32
	0.8–5.0	0.477	21	2.06	0.318	33	2.19
0.08–0.11	0.0–0.25	0.145	21	2.06	0.052	35	2.33
	0.25–0.5	0.151	36	3.54	0.093	29	1.93
	0.5–0.8	0.242	12	1.18	0.154	19	1.26
	0.8–5.0	0.496	5	0.49	0.447	12	0.8
0.11–0.25	0.0–0.25	0.072	5	0.49	0.029	3	0.2
	0.25–0.5	0.132	13	1.28	0.079	6	0.4
	0.5–0.8	0.164	5	0.49	0.202	1	0.07
	0.8–5.0	0.607	5	0.49	0.470	2	0.13

For low albedo with low AOD ranges (albedo 0.0–0.05, AOD 0.0–0.25; albedo 0.05–0.08, AOD 0.0–0.25; albedo 0.05–0.08, AOD 0.25–0.5; albedo 0.05–0.08, AOD 0.5–0.8) the GEMS RMSE (0.087, 0.117, 0.140, and 0.212) was lower than that of MODIS DT AOD (0.123, 0.142, 0.153, and 0.250), respectively. In the lowest surface albedo (0.0–0.05) and AOD (0.0–0.25) ranges, the GEMS RMSE (0.087) is lower than that of MODIS DT (0.123). For GEMS, the aerosol algorithm uses UV channels in the inversion procedure, where Rayleigh signals predominate over surface-reflectance signals, so GEMS AOD products are less affected by surface-reflectance variations. However, the data number percentage of GEMS AOD (15.93%) is lower than that of MODIS DT products (23.97%), indicating that the GEMS aerosol algorithm sometimes retrieves negative AOD for very clear regions. When AOD values are very low, TOA reflectance difference values (e.g., TOA reflectance difference between AOD of 0.0 and 0.1) are very low. Therefore, both the combination of inaccurate aerosol-type assumptions and the over-compensation of Rayleigh scattering or overestimation of surface albedo may cause this negative AOD problem, which required further assessment.

4.3.2. Validation Results

Results of a case study of AOD data fusion on 24 March 2018, are shown in Figure 9. On that day, MODIS RGB data indicated aerosol plumes over eastern China with clouds over the ocean as shown in the MODIS RGB image of Figure 9a, while there were low aerosol concentrations over northwestern China. GEMS 443 nm AOD data simulated with OMI L1B are shown in Figure 9c. OMI has row-anomaly issues in the middle part of the across-track sequence, and is thus not suitable for aerosol retrievals [36]. MODIS DT C6.1 550 nm AOD products are shown in Figure 9d. MODIS DT uses visible channels for retrieval, so does not retrieve aerosol properties over bright surfaces as shown in Figure 9d. Fused 550 nm AOD products are shown in Figure 9b, based on extrapolation of 443 nm GEMS AOD to 550 nm using selected aerosol model assumptions. Over bright surface areas, GEMS aerosol products were used. For the aerosol plume area, GEMS and MODIS DT aerosol products were fused using the MLE method. The western coast of the Korean Peninsula was within the sun-glint area for both OMI and MODIS instruments, so aerosol data were not retrieved. The fused 550 nm AOD products exhibit smooth and consistent spatial distributions compared with the original individual AOD products, implying that the ranges of AOD and surface albedo are well established. If the two ranges were not well established, the spatial distribution of the fused AOD products would have been rugged and uneven.

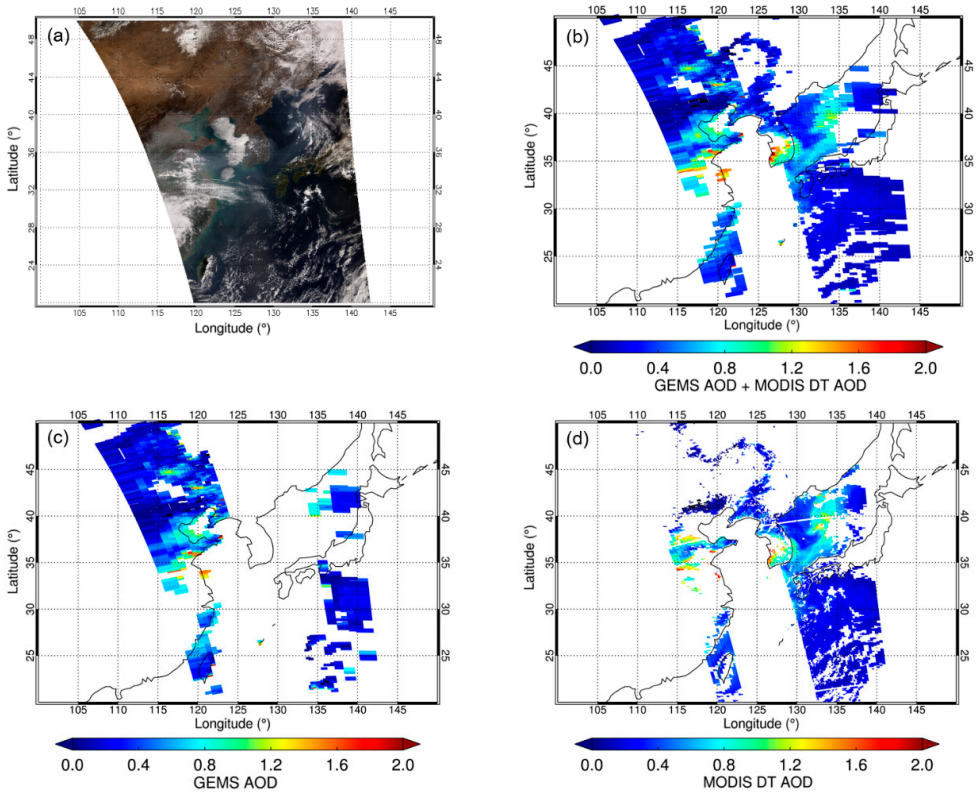

Figure 9. (**a**) MODIS RGB data for 24 March 2018. (**b**) Merged 550 nm AOD products for GEMS and MODIS DT AOD (C6.1) based on the maximum likelihood estimation (MLE) method. (**c**) GEMS 550 nm AOD products (using L1B of OMI as a proxy). The MODIS high-resolution cloud mask was used to screen cloud data in GEMS AOD. (**d**) MODIS DT 550 nm AOD (C6.1) product.

Validation results for GEMS AOD (using OMI L1B as a proxy), MODIS DT AOD, and fused AOD products are shown in Figure 10; Figure 10b,d,f indicate corresponding normalized frequency histograms of AOD bias. The fused AOD products have accuracies comparable with MODIS DT AOD products, with an increasing number of data points. Moreover, the AOD bias distribution of fused AOD products have distributions similar to those of MODIS DT AOD products. From the

perspective of GEMS AOD (Figure 10a), the merged products (Figure 10e) produced better statistics overall, with increasing slope (from 0.618 to 0.776; Figure 10a,e), decreasing offset (from 0.184 to 0.112), increasing correlation coefficients (from 0.883 to 0.887), decreasing RMSE (from 0.234 to 0.205), and increasing Q (from 59.31% to 69.79%), with an increasing number of total validation points (from 548 to 1066). Fused results are thus beneficial for GEMS AOD in terms of increasing accuracy and spatial coverage. Furthermore, compared with the OMAERUV AOD product, fusion may provide a straightforward means of validation as the discarding of data with SD > 0.3 (to mitigate possible sub-pixel cloud contamination [65]) is avoided.

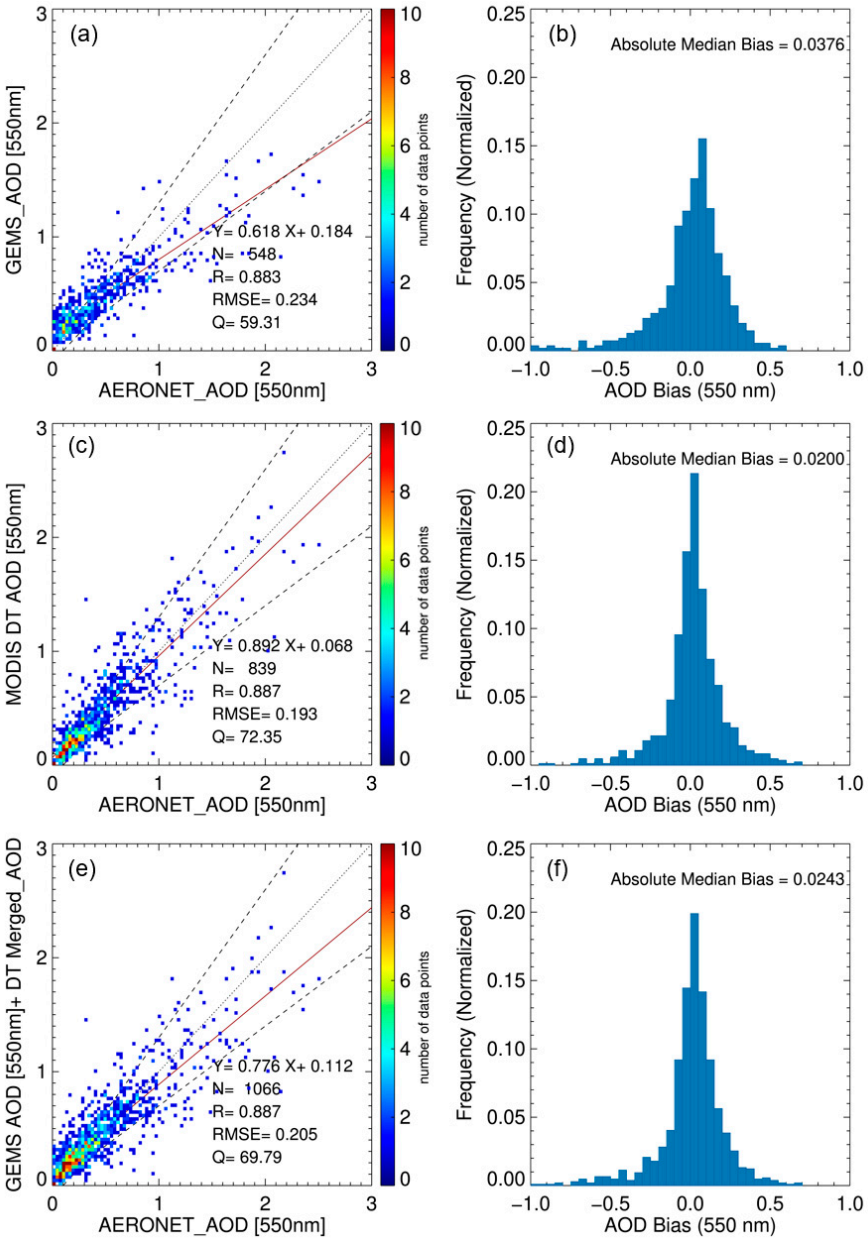

Figure 10. (**a**) Validation results for GEMS AOD (using L1B of OMI as a proxy), 2006. (**b**) Normalized frequency histogram of AOD bias corresponding to results (**a**). (**c**) Validation results for MODIS DT AOD, 2006. (**d**) Normalized frequency histogram of AOD bias corresponding to results (**c**). (**e**) Validation of fused AOD products, 2006. (**f**) Normalized frequency histogram of AOD bias corresponding to the results (**e**). Dotted and dashed lines in (**a**,**c**,**e**) are 1:1 and expected AOD error (30% or 0.1; Ahn et al. [65]) lines. The red line indicates the linear fitting line of validation results. The corresponding slope (A) and offset (B) for the red line are presented in each figure in $y = Ax + B$ format.

Ratios of retrieved pixels to total measurement L1B pixels for each original AOD product and the fused AOD dataset are plotted in Figure 11. Both GEMS AOD (using OMI L1B as a proxy) and MODIS DT products had high data availability in autumn and low availability in summer due to low and high cloud fractions, respectively. GEMS AOD products had better spatial coverage, especially during autumn and winter. The fused products displayed better spatial data availability than each source AOD product.

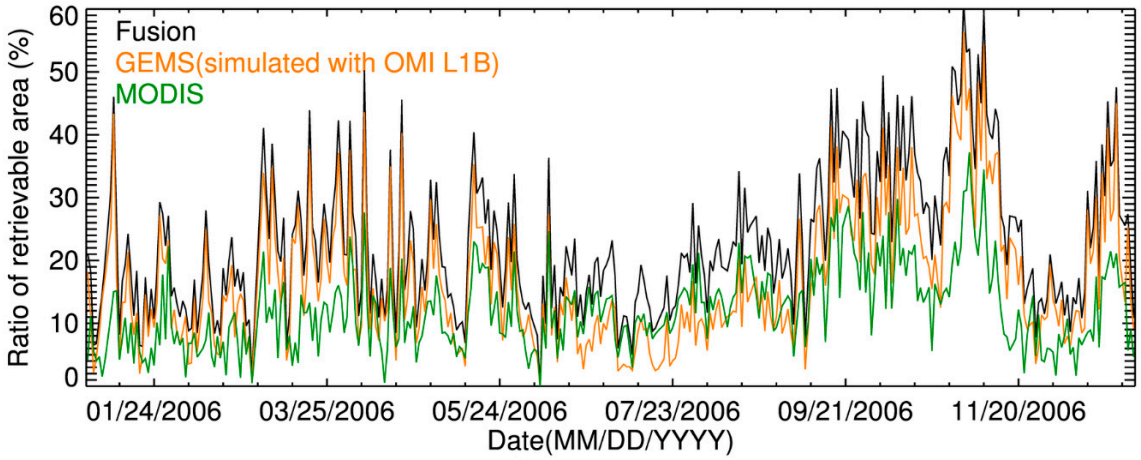

Figure 11. Ratio of retrieved area for fused AOD dataset and source AOD products for 1 January to 31 December 2006.

5. Error Analysis before and after Synergistic Meteorological Imager Use

Error analyses were undertaken for GEMS AOD before and after aerosol fusion with results presented in Figures 12 and 13, which show GEMS AOD bias with respect to parameters related to the inversion procedure. The scattering angle, calculated from OMI measurement geometry for each pixel, is considered in Figure 12a, and AE values are plotted in Figure 12b as indicators of aerosol size, calculated from AERONET AOD at 440 and 675 nm. The bias with respect to surface reflectance and the OMI surface climatology database [64] at 443 nm are plotted in Figure 13a, as used here in the GEMS AOD inversion procedure, and AERONET AOD is plotted against GEMS-AERONET AOD in Figure 13b. In Figures 12 and 13, the blue color represents GEMS AOD simulated with OMI L1B data, and the red color indicates the fused AOD dataset, with each bin representing the median and SD of 40 collocated GEMS AOD (using OMI L1B as a proxy) and AERONET data points. Overall, bias analysis indicates decreased absolute median bias (AMB) for all related parameters: 0.0549 to 0.0239 for scattering angle; 0.0241 to 0.0044 for AE; 0.0612 to 0.0232 for surface reflectance; 0.0612 to 0.0344 for AOD. The AMB and bin median and bias values decreased after merging of the AOD products.

The greatest decrease in bias occurred in the backscattering geometry (Figure 12a). Physically, the same surface may appear brighter in backscattering geometry than in forward scattering geometry. The GEMS bias in backscattering geometry may be caused by our use of the Kleipool dataset [64], which is a monthly composited dataset excluding geometry consideration. The MODIS DT algorithm takes into account the angular effect (scattering angle) in surface reflectance estimation, so the backscattering error might have decreased after fusion with MODIS DT. This suggests that surface reflectance, rather than the Kleipool dataset, should be developed further for use with GEMS.

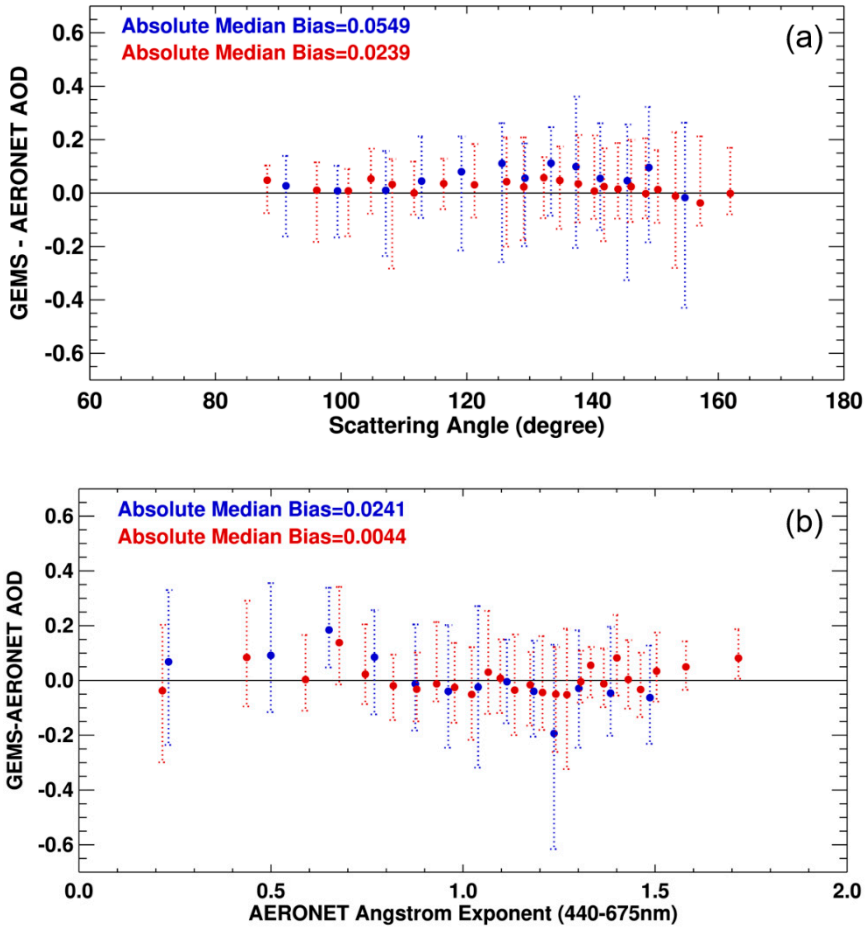

Figure 12. (**a**) The bias of GEMS AOD with respect to scattering angle. (**b**) The bias of GEMS AOD with respect to collocated AERONET Ångström exponent (440–675 nm). Blue and red refer to before and after aerosol fusion, respectively. The absolute median bias (AMB) was calculated for the total collocated blue and red points. Circles and bars represent median and SD values for 40 collocated points of GEMS and AERONET data.

The AOD bias did not change significantly over the AE range of 0.7–1.3 (Figure 12b), which indicates that neither GEMS nor MODIS DT has large errors in the median size. The bias at low AE (0.5–0.7, corresponding to coarse particles) decreased, and that at high AE (1.3–1.8) slightly increased. This suggests that the two AODs are mixed, with the bias being fused evenly in terms of particle size. Figure 13a indicates that the bias decreased evenly over the entire section of surface reflection, implying that the surface reflectance range used in Equation (4) was set correctly. In Figure 13b, the bias approaches zero over the entire AOD range after fusion. At incredibly low AOD (0.0–0.2), there was a bias of 0.1–0.2 for GEMS, which decreased after fusion. The RMSE of GEMS AOD in Table 5 was 0.087 for *BSA* 0.0–0.05 and AOD 0.0–0.25; 0.117 for *BSA* 0.05–0.08 and AOD 0.0–0.25; 0.145 for *BSA* 0.08–0.11 and AOD 0.0–0.25. When considering the GEMS AOD bias with respect to the scattering angle (Figure 12a), it is possible to infer the bias largely from the backscattering geometry, and this point should be investigated in future applications of the GEMS aerosol algorithm.

The MLE method uses RMSE as a weighting factor, so more accurate satellite results are reflected in fusion AOD results with a large fraction. Validation results might be improved significantly if the merged AOD were based on the more accurate AOD data from the two satellites without applying the RMSE weighting factor, although the AOD spatial distribution could have significant discontinuities. The advantage of the MLE method is therefore that the errors of the two satellites can be considered using RMSE, and it is possible to calculate the merged AOD with minimal spatial discontinuity. The disadvantage, however, is the assumption that all outputs have a bias of zero. If the merged AOD

was calculated after correction of the AOD bias from each satellite L2 AOD product, more accurate satellite output could be obtained.

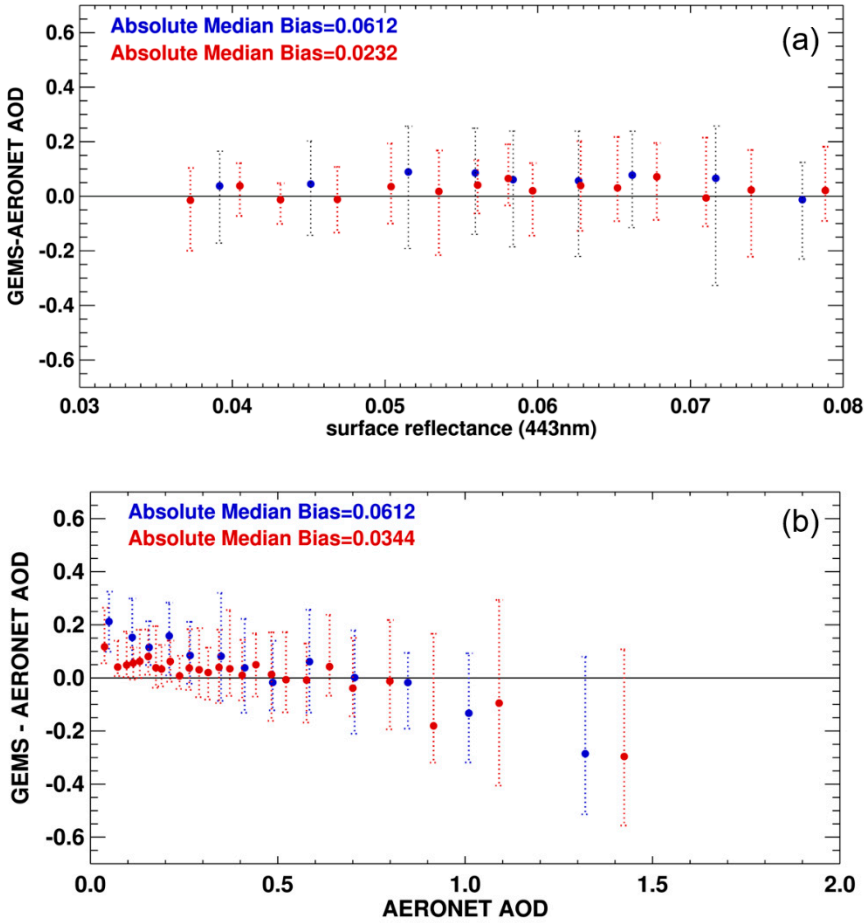

Figure 13. (**a**) Bias of GEMS AOD with respect to surface reflectance (443 nm), as used for AOD retrieval. (**b**) Bias of GEMS AOD with respect to collocated AERONET AOD direct-measurement data (L2). Blue and red refer to before and after aerosol fusion, respectively. The AMB was calculated for the total collocated blue and red points. Circles and bars represent median and SD values for 40 collocated data points for GEMS and AERONET data.

6. Discussion

In this study, we presented a method for synergistic use of hyperspectral UV–visible and MI data to improve aerosol retrieval products and to produce optimal AOD datasets. The proposed methods were simulated using OMI and MODIS data, which can be proxies for GEMS and AMI data, highlighting improvements in aerosol results. The methodology presented here is generally applicable to other UV–visible instruments and meteorological satellites. Previous studies generally aimed to improve aerosol retrieval products [12–19], or to create 'best' AOD datasets by merging individual AOD products [20–25] to provide users with optimal AOD data for points observed simultaneously by multiple satellites.

With regard to cloud masking, if clouds are much smaller than the pixel spatial resolution their signals cannot be distinguished from aerosol signals. For example, a thin cloud with a resolution of 500 m is clearly visible in satellite RGB systems with a resolution of 500 m, but is indistinguishable with a spatial resolution of 10 km. Many UV–visible instruments have spatial resolutions of >3.5 km and may have sub-pixel cloud contamination issues that affect validation results. We have shown that it is possible to separate clouds more accurately using high-resolution MI cloud data for observations of the same location. As the cloud fraction in the AOD pixel decreased from 80% to 20%, the AOD

correlation coefficient increased from 0.786 to 0.871. Our method is thus beneficial for reducing the inconvenience of discriminating clouds in the validation stage by data SD, and for determining where the clouds are in the aerosol retrieval region.

We have also proposed a new method for applying the TDCI algorithm to UV–visible instrument aerosol retrieval processes, based on IR data being suitable for DS discrimination. Statistical analysis indicates that GEMS DS aerosol detection accuracy was improved from 72% to 94% using TDCI for aerosol type selection. In addition, SSA results were improved particularly for aerosol types BC and DS. UV–visible instruments generally face the difficulty of accurately separating aerosol size information when retrieving aerosol data. It is difficult to accurately determine the aerosol type from nadir-view satellites, owing to their low information content, but it is possible to determine aerosol size or absorption information within a large group aerosol type from wavelength-dependent aerosol optical properties. Torres et al. [13] provided a novel method for using AIRS CO as a tracer of smoke and for its application in the aerosol retrieval algorithm. However, since neither GEMS nor AMI can obtain CO data, the method is difficult to apply. After synergistic use of MI at the algorithm stage, we have shown that fused AOD data may provide spatially wider AOD with consistent accuracy. If a problem occurs with a payload, another satellite can compensate spatially. Here, only uncertainties at pixel-level were considered for the output of AOD, and this could be improved if the bias characteristics of each output were utilized.

In this study, the LEO OMI and MODIS instruments were used as proxy datasets for GEMS and AMI. OMI and MODIS have points in common with GEMS and AMI, such as FWHM, spectral sampling, and wavelength, but there are also differences in temporospatial resolution and instrument errors. Previous studies indicated that the OMI operational aerosol algorithm (OMAERUV) can be tested using the Global Ozone Monitoring Experiment (GOME) L1B as pre-launch product validation (OMI Algorithm Theoretical Basis Document (ATBD) [67]) [68,69]. The OMAERUV algorithm has an established accuracy (~30%) based on heritage TOMS validation results [67,70]. The MODIS DT aerosol algorithm also exhibited the expected algorithm errors of $\pm(0.03 + (0.05 \times \mathrm{AOD}))$ over ocean and $\pm(0.05 + (0.15 \times \mathrm{AOD}))$ over land in the pre-launch Tropospheric Aerosol Radiative Forcing Observational Experiment (TARFOX) through use of a MODIS airborne simulator (MAS) aboard the NASA ER-2 satellite [71–73]. OMI and MODIS satisfy the 30% and expected algorithm error of $\pm(0.05 + (0.15 \times \mathrm{AOD}))$ after launch, as set pre-launch [20,65]. Of course, algorithm accuracy generally depends on payload calibration accuracy [20,40,41].

It is well known that the main sources of error in aerosol products are cloud contamination, errors in the assumed (or retrieved) surface reflectivity, instrumental errors, and errors in the aerosol models (in forward modeling) [67]. For instrument errors, aerosol product accuracy is affected by radiometric calibration errors such as radiometric calibration offsets, radiometric calibration scale factors, and radiometric noise, rather than spectral calibration errors.

Errors due to cloud contamination depend mainly on the observed spatial resolution, as mentioned in Sections 1 and 4.1. In the case of surface reflectivity, monthly reflectivity climatology or surface reflectance estimated from the IR channel is primarily used, as derived from the payload [9,20,29,64,74]. If it is not available at the launch stage, the algorithm can rely on existing surface climatology [64]. The aerosol model used in forward modeling does not require a change of payload; therefore, we anticipate that an aerosol algorithm tested before satellite launch will rely on the calibration state of the payload after launch, except for a slight threshold modification for cloud screening and re-calculation of surface reflectivity. The algorithm performance itself will not change significantly.

As an example, the GOCI aerosol algorithm (operational since 2010; cf. Table 1) was tested using MODIS L1B before launch. With MODIS L1B, the correlation coefficient between AERONET AOD and the GOCI AOD products was 0.78–0.92 for the Gosan and Shirahama sites [75]. After GOCI launch, the correlation coefficient between AERONET AOD and the GOCI AOD products was ~0.8 over the field of regard [76]. Changes were in the refinement of cloud screening, turbid-water detection, and surface reflectivity over time. The original frame of the algorithm has not changed. In changing

from LEO to GEO satellites, the major change in the aerosol algorithm is the reconstruction of surface reflectivity. In the case of the GOCI, surface reflectance was changed to a method composited by time, with a 30-day minimum for calculation of MODIS (because surface reflectivity depends on geometry).

In considering the results of previous studies with respect to the present study, high-resolution AMI data can be applied for cloud screening provided there is no major problem with GEMS or AMI calibration, and the GEMS aerosol algorithm should yield stable aerosol data even over bright surfaces. Because the shortest wavelength band in AMI is 470 nm, it may have a higher AOD uncertainty than GEMS over bright surfaces. The TDCI index can be re-determined only by adjusting the threshold. Therefore, if the SD (Equation (4)) with respect to AOD and surface reflectivity is selected, the final merged aerosol product may increase the overall spatial coverage while also complementing the uncertainty of each satellite AOD product.

For TDCI calculations, we used MODIS L1B C6 data, while the most recent MODIS L1B dataset is C6.1. However, of the three MODIS bands examined, only Terra MODIS band 29 (8.55 μm) exhibits any difference between the MODIS C6- and C6.1-based results [77], so the use of C6 would rarely affect the significance of our results. This study explored the possibility of constructing an optimal aerosol dataset by the synergistic use of GEMS, hyperspectral UV–visible instruments, AMI, and broadband MI. Future studies should focus on the application of these possibilities with new geostationary satellites such as GEMS, TEMPO, Sentinel-4, AHI, AMI, and ABI.

The improved aerosol products developed through the fusion of AOD products can be used to monitor air quality and improve air-quality forecasting accuracy over East Asia. Previous particulate-matter estimation studies have indicated that satellite AOD coverage and aerosol product accuracy may affect the accuracy of predicted $PM_{2.5}$ (particulate matter of diameter < 2.5 μm). Sorek-Hamer et al. [78] used MODIS DB AOD products and combined DB–DT algorithm AOD products to better predict $PM_{2.5}$ concentrations over bright surfaces. Bilal et al. [79] processed to find the best of AOD among aerosol products of SARA, DT, and DB since the accuracy of AOD affects the accuracy of $PM_{2.5}$. Moreover, Song et al. [80] found that a high sampling rate for AOD data with unbiased sampling is preferable for estimating surface $PM_{2.5}$ concentrations, with $PM_{2.5}$ estimates differing, on average, by 11.2 μg m^{-3} in autumn and 8.5 μg m^{-3} in winter after including AOD data over bright surfaces. Methods developed here may aid hourly prediction of surface $PM_{2.5}$ concentrations.

The aerosol algorithm improved in this study may also contribute to trace-gas retrieval data. Trace-gas data are retrieved using a hyperspectral spectrometer that can detect cross-sectional features. If AOD, SSA, and ALH data could be obtained from the same sensor, the temporospatial collocation errors of other satellites could be reduced.

7. Conclusions

The main purpose of this study was to generate an optimal aerosol dataset by the synergistic use of hyperspectral UV–visible instruments and broadband MI. The procedure involves the overcoming of physical limitations of GEMS aerosol algorithms in terms of aerosol size insensitivity and cloud masking by using MI and merging of aerosol data between improved GEMS and MI aerosol products.

MI IR measurements are useful for cirrus cloud masking of GEMS aerosol retrievals. The high spatial resolutions of MI TOA reflectance data together with IR data are helpful for refining sub-pixel cloud masking, which is difficult for GEMS. In terms of improvements in aerosol type classification, statistical analysis indicates that GEMS DS aerosol detection accuracy improved from 72% to 94% using TDCI for DS selection. Application of TDCI in the detection of DS in the GEMS aerosol retrieval procedure improved SSA results, particularly for aerosol types of BC and DS, which is consistent with results of the theoretical sensitivity test of the GEMS aerosol algorithm in terms of aerosol-type misclassification. Due to the advantage of retrieving aerosols over bright surfaces from the UV–visible channel, the fused AOD products exhibit better spatial data availabilities than any of the AOD source products, with an accuracy matching that of source products. AMB values for scattering angle, surface reflectance, AE, and AERONET AOD are all significantly improved.

The improved aerosol retrieval algorithm presented in this study is applicable to the GEMS aboard the GEO-KOMPSAT-2B satellite and AMI aboard the GEO-KOMPSAT-2A satellite, which were launched in February 2020 and December 2018, respectively. The synergistic use of MI data indicates the future possibility of improving GEMS aerosol algorithms and constructing optimal aerosol datasets.

Author Contributions: Conceptualization, S.G., J.K., S.S.P., M.K., J.-Y.K., D.-W.L. and J.I.; methodology, S.G., J.K., S.S.P., M.K. and H.L.; software, S.G., J.K., S.S.P., M.K. and H.L.; validation, S.G. and S.S.P.; formal analysis, S.G., S.S.P., M.K. and H.L.; investigation, S.G., J.K., S.S.P., M.K., H.L., J.-Y.K., D.-W.L. and J.I.; resources, S.G., J.K., S.S.P., M.K. and H.L.; data curation, S.G. and S.S.P.; writing—original draft preparation, S.G. and J.K.; writing—review and editing, All Authors.; visualization, S.G.; supervision, J.K.; project administration, J.K.; funding acquisition, J.K., J.-Y.K., D.-W.L. and J.I. All authors have read and agreed to the published version of the manuscript.

Funding: National Institute of Environment Research (NIER) : NIER-2018-01-02-032 Korea Ministry of Environment (MOE) under the Public Technology Program based on Environmental Policy : 2017000160001.

Acknowledgments: The author would like to acknowledge the support provided by the Korea Ministry of Environment (MOE) under the Public Technology Program based on Environmental Policy (2017000160001). Also, the author would like to acknowledge the support provided by the National Institute of Environment Research (NIER), supported by the Ministry of Environment (MOE) of the Republic of Korea (NIER-2018-01-02-032). Finally, we thank the reviewers for their suggestions, which improved the manuscript.

Conflicts of Interest: The authors declare no conflict of interest.

Appendix A

List of acronyms

AAE	Absorption Ångström exponent
AATSR	Advanced Along-Track Scanning Radiometer
ABI	Advanced Baseline Imager
AE	Ångström exponent
AERONET	Aerosol Robotic Network
AGRI	Advanced Geostationary Radiation Imager
AHI	Advanced Himawari Imager
AIRS	Atmospheric InfraRed Sounder
ALH	Aerosol layer height
AMB	Absolute median bias
AMI	Advanced Meteorological Imager
AOD	Aerosol optical depth
ATBD	Algorithm Theoretical Basis Document
BC	Absorbing fine pollution particles (type)
BME	Bayesian Maximum Entropy
BRDF	bidirectional reflectance distribution function
BSA	Black sky albedo
C5	Collection 5
C6	Collection 6
C6.1	Collection 6.1
CALIOP	Cloud-Aerosol Lidar with Orthogonal Polarization
CALIPSO	Cloud-Aerosol Lidar and Infrared Pathfinder Satellite Observation
CCD	Charge-coupled device
CO	Carbon monoxide
DB	Deep blue
DS	Dust (type)
DT	Dark target
ECV	Essential climate variables
ESR	Estimated surface reflectance
FD	Full disk
FMF	Fine mode fraction
FOR	Field of regard

GCOS	Global Climate Observing System
GEMS	Geostationary Environment Monitoring Spectrometer
GEO	Geostationary Earth orbit
GEO-KOMPSAT-2A	Geostationary Korea Multi-Purpose Satellite 2A
GEO-KOMPSAT-2B	Geostationary Korea Multi-Purpose Satellite 2B
GOCI	Geostationary Ocean Color Imager
GOCI-2	Geostationary Ocean Color Imager-2
GOME	Global Ozone Monitoring Experiment
HCHO	Formaldehyde
IR	Infrared
KARI	Korea Aerospace Research Institute
KMA	Korea Meteorological Administration
L1B	Level 1B
L2	Level 2
LEO	Low Earth orbit
LER	Lambertian equivalent reflectivity
LUT	Look-up table
MAIAC	Multi-Angle Implementation of Atmospheric Correction
MAS	MODIS airborne simulator
MI	Meteorological Imager
MISR	Multi-angle imaging spectroradiometer
MLE	Maximum likelihood estimation
MODIS	Moderate Resolution Imaging Spectroradiometer
MRM	Minimum reflectivity method
NA	Non-absorbing (type)
NDVI	Normalized difference vegetation index
NIR	Near-infrared
NO_2	Nitrogen dioxide
O_3	Ozone
OE	Optimal estimation
OI	Optimal interpolation
OMI	Ozone Monitoring Instrument
OMPS	Ozone Mapping Profiler Suite
$PM_{2.5}$	Particulate matter
POCD	Probability of correct detection
POFD	Probability of false positive detection
RGB	Red–Green–Blue
RMSE	Root mean square error
SAFARI 2000	Southern African Regional Science Initiative
SD	Standard deviation
SeaWiFS	Sea-Viewing Wide Field-of-View Sensor
SNR	Signal to noise ratio
SO_2	Sulfur dioxide
SSA	Single scattering albedo
TARFOX	Tropospheric Aerosol Radiative Forcing Observational Experiment
TDCI	Total dust confidence index
TEMPO	Tropospheric Emissions: Monitoring of Pollution
TOA	Top of atmosphere
TOMS	Total Ozone Mapping Spectrometer
UV	Ultraviolet
UVAI	Ultraviolet aerosol index
UV-MFRSR	UV Multi-Filter Rotating Shadowband Radiometer
VIIRS	Visible Infrared Imaging Radiometer Suite
VISAI	Visible aerosol index
VSD	Volume size distribution

References

1. Griggs, M. Measurements of atmospheric aerosol optical thickness over water using ERTS-1 data. *J. Air Pollut. Control. Assoc.* **1975**, *25*, 622–626. [CrossRef] [PubMed]
2. King, M.D.; Kaufman, Y.J.; Tanré, D.; Nakajima, T. Remote Sensing of Tropospheric Aerosols from Space: Past, Present, and Future. *Bull. Am. Meteorol. Soc.* **1999**, *80*, 2229–2259. [CrossRef]
3. Lee, K.H.; Li, Z.; Kim, Y.J.; Kokhanovsky, A. *Atmospheric Aerosol Monitoring from Satellite Observations: A History of Three Decades, Atmospheric and Biological Environmental Monitoring*; Springer: Dordrecht, The Netherlands, 2009; pp. 13–38.
4. IPCC. *Climate Change 2013: The Physical Science Basis: Working Group I Contribution to the Fifth Assessment Report of the Intergovernmental Panel on Climate Change*; Cambridge University Press: Cambridge, UK; New York, NY, USA, 2013; p. 1535.
5. Zoogman, P.; Liu, X.; Suleiman, R.; Pennington, W.; Flittner, D.; Al-Saadi, J.; Hilton, B.; Nicks, D.; Newchurch, M.; Carr, J. Tropospheric emissions: Monitoring of pollution (TEMPO). *J. Quant. Spectrosc. Radiat. Transf.* **2017**, *186*, 17–39. [CrossRef] [PubMed]
6. Kim, J.; Jeong, U.; Ahn, M.-H.; Kim, J.H.; Park, R.J.; Lee, H.; Song, C.H.; Choi, Y.-S.; Lee, K.-H.; Yoo, J.-M.; et al. New era of air quality monitoring from space: Geostationary Environment Monitoring Spectrometer (GEMS). *Bull. Am. Meteorol. Soc.* **2020**, *101*, E1–E22. [CrossRef]
7. Gulde, S.; Kolm, M.; Smith, D.; Maurer, R.; Courrèges-Lacoste, G.B.; Sallusti, M.; Bagnasco, G. Sentinel 4: A geostationary imaging UVN spectrometer for air quality monitoring: Status of design, performance and development. In Proceedings of the International Conference on Space Optics—ICSO 2014, International Society for Optics and Photonics, Tenerife, Spain, 6–10 October 2014; SPIE: Bellingham, WA, USA, 2017; p. 1056341.
8. Yang, J.; Zhang, Z.; Wei, C.; Lu, F.; Guo, Q. Introducing the new generation of Chinese geostationary weather satellites, Fengyun-4. *Bull. Am. Meteorol. Soc.* **2017**, *98*, 1637–1658. [CrossRef]
9. Lim, H.; Choi, M.; Kim, J.; Kasai, Y.; Chan, P.W. AHI/Himawari-8 Yonsei aerosol retrieval (YAER): Algorithm, validation and merged products. *Remote Sens.* **2018**, *10*, 699. [CrossRef]
10. Laszlo, I.; Ciren, P.; Liu, H.; Kondragunta, S.; Tarpley, J.D.; Goldberg, M.D. Remote sensing of aerosol and radiation from geostationary satellites. *Adv. Space Res.* **2008**, *41*, 1882–1893. [CrossRef]
11. Choi, Y.-S.; Ho, C.-H. Earth and environmental remote sensing community in South Korea: A review. *Remote Sens. Appl. Soc. Environ.* **2015**, *2*, 66–76. [CrossRef]
12. Kim, J.; Lee, J.; Lee, H.C.; Higurashi, A.; Takemura, T.; Song, C.H. Consistency of the aerosol type classification from satellite remote sensing during the Atmospheric Brown Cloud–East Asia Regional Experiment campaign. *J. Geophys. Res. Atmos.* **2007**, *112*. [CrossRef]
13. Torres, O.; Ahn, C.; Chen, Z. Improvements to the OMI near-UV aerosol algorithm using A-train CALIOP and AIRS observations. *Atmos. Meas. Tech.* **2013**, *6*, 3257–3270. [CrossRef]
14. Vermote, E.F.; Roger, J.-C.; Sinyuk, A.; Saleous, N.; Dubovik, O. Fusion of MODIS-MISR aerosol inversion for estimation of aerosol absorption. *Remote Sens. Environ.* **2007**, *107*, 81–89. [CrossRef]
15. Jeong, M.-J.; Li, Z. Quality, compatibility, and synergy analyses of global aerosol products derived from the advanced very high resolution radiometer and Total Ozone Mapping Spectrometer. *J. Geophys. Res.* **2005**, *110*, D10S08. [CrossRef]
16. Jeong, M.J.; Hsu, N.C. Retrievals of aerosol single-scattering albedo and effective aerosol layer height for biomass–burning smoke: Synergy derived from "A-Train" sensors. *Geophys. Res. Lett.* **2008**, 35. [CrossRef]
17. Lee, J.; Hsu, N.C.; Bettenhausen, C.; Sayer, A.M.; Seftor, C.J.; Jeong, M.J. Retrieving the height of smoke and dust aerosols by synergistic use of VIIRS, OMPS, and CALIOP observations. *J. Geophys. Res. Atmos.* **2015**, *120*, 8372–8388. [CrossRef]
18. Satheesh, S.; Torres, O.; Remer, L.; Babu, S.S.; Vinoj, V.; Eck, T.; Kleidman, R.; Holben, B. Improved assessment of aerosol absorption using OMI-MODIS joint retrieval. *J. Geophys. Res. Atmos.* **2009**, *114*. [CrossRef]
19. Eswaran, K.; Satheesh, S.K.; Srinivasan, J. Multi-satellite retrieval of single scattering albedo using the OMI–MODIS algorithm. *Atmos. Chem. Phys.* **2019**, *19*, 3307–3324. [CrossRef]
20. Levy, R.; Mattoo, S.; Munchak, L.; Remer, L.; Sayer, A.; Patadia, F.; Hsu, N. The Collection 6 MODIS aerosol products over land and ocean. *Atmos. Meas. Tech.* **2013**, *6*, 2989–3034. [CrossRef]

21. Xue, Y.; Xu, H.; Guang, J.; Mei, L.; Guo, J.; Li, C.; Mikusauskas, R.; He, X. Observation of an agricultural biomass burning in central and east China using merged aerosol optical depth data from multiple satellite missions. *Int. J. Remote Sens.* **2014**, *35*, 5971–5983. [CrossRef]
22. Tang, Q.; Bo, Y.; Zhu, Y. Spatiotemporal fusion of multiple-satellite aerosol optical depth (AOD) products using Bayesian maximum entropy method. *J. Geophys. Res. Atmos.* **2016**, *121*, 4034–4048. [CrossRef]
23. Xu, H.; Guang, J.; Xue, Y.; De Leeuw, G.; Che, Y.; Guo, J.; He, X.; Wang, T. A consistent aerosol optical depth (AOD) dataset over mainland China by integration of several AOD products. *Atmos. Environ.* **2015**, *114*, 48–56. [CrossRef]
24. Xie, Y.; Xue, Y.; Che, Y.; Guang, J.; Mei, L.; Voorhis, D.; Fan, C.; She, L.; Xu, H. Ensemble of ESA/AATSR aerosol optical depth products based on the likelihood estimate method with uncertainties. *IEEE Trans. Geosci. Remote Sens.* **2017**, *56*, 997–1007. [CrossRef]
25. Lee, J.; Hsu, N.C.; Sayer, A.M.; Seftor, C.J.; Kim, W.V. Aerosol Layer Height with Enhanced Spectral Coverage Achieved by Synergy Between VIIRS and OMPS-NM Measurements. *IEEE Geosci. Remote Sens. Lett.* **2020**, 1–5. [CrossRef]
26. Lyapustin, A.; Wang, Y.; Korkin, S.; Kahn, R.; Winker, D. MAIAC thermal technique for smoke injection height from MODIS. *IEEE Geosci. Remote Sens. Lett.* **2019**, *17*, 730–734. [CrossRef]
27. Kim, J.; Kim, M.; Choi, M. *Monitoring Aerosol Properties in East Asia from Geostationary Orbit: GOCI, MI and GEMS, Air Pollution in Eastern Asia: An Integrated Perspective*; Springer: Cham, Switzerland, 2017; pp. 323–333.
28. Remer, L.; Mattoo, S.; Levy, R.; Heidinger, A.; Pierce, R.; Chin, M. Retrieving aerosol in a cloudy environment: Aerosol product availability as a function of spatial resolution. *Atmos. Meas. Tech.* **2012**, *5*, 1823–1840. [CrossRef]
29. Choi, M.; Kim, J.; Lee, J.; Kim, M.; Park, Y.-J.; Holben, B.; Eck, T.F.; Li, Z.; Song, C.H. GOCI Yonsei aerosol retrieval version 2 products: An improved algorithm and error analysis with uncertainty estimation from 5-year validation over East Asia. *Atmos. Meas. Tech.* **2018**, *11*, 385–408. [CrossRef]
30. Levy, R.C.; Remer, L.A.; Mattoo, S.; Vermote, E.F.; Kaufman, Y.J. Second–generation operational algorithm: Retrieval of aerosol properties over land from inversion of Moderate Resolution Imaging Spectroradiometer spectral reflectance. *J. Geophys. Res. Atmos.* **2007**, *112*. [CrossRef]
31. Lee, J.; Kim, J.; Song, C.; Kim, S.; Chun, Y.; Sohn, B.; Holben, B. Characteristics of aerosol types from AERONET sunphotometer measurements. *Atmos. Environ.* **2010**, *44*, 3110–3117. [CrossRef]
32. Jethva, H.; Torres, O.; Ahn, C. Global assessment of OMI aerosol single–scattering albedo using ground–based AERONET inversion. *J. Geophys. Res. Atmos.* **2014**, *119*, 9020–9040. [CrossRef]
33. Go, S.; Kim, J.; Mok, J.; Irie, H.; Yoon, J.; Torres, O.; Krotkov, N.A.; Labow, G.; Kim, M.; Koo, J.-H. Ground-based retrievals of aerosol column absorption in the UV spectral region and their implications for GEMS measurements. *Remote Sens. Environ.* **2020**, *245*, 111759. [CrossRef]
34. Levelt, P.F.; van den Oord, G.H.; Dobber, M.R.; Malkki, A.; Visser, H.; de Vries, J.; Stammes, P.; Lundell, J.O.; Saari, H. The ozone monitoring instrument. *IEEE Trans. Geosci. Remote. Sens.* **2006**, *44*, 1093–1101. [CrossRef]
35. Levelt, P.F.; Joiner, J.; Tamminen, J.; Veefkind, J.P.; Bhartia, P.K.; Carn, S. The Ozone Monitoring Instrument: Overview of 14 years in space. *Atmos. Chem. Phys.* **2018**, *18*, 5699–5745. [CrossRef]
36. Schenkeveld, V.E.; Jaross, G.; Marchenko, S.; Haffner, D.; Kleipool, Q.L.; Rozemeijer, N.C.; Veefkind, J.P.; Levelt, P.F. In-flight performance of the Ozone Monitoring Instrument. *Atmos. Meas. Tech.* **2017**, *10*, 1957–1986. [CrossRef] [PubMed]
37. Kim, M.; Kim, J.; Torres, O.; Ahn, C.; Kim, W.; Jeong, U.; Go, S.; Liu, X.; Moon, K.J.; Kim, D.-R. Optimal estimation-based algorithm to retrieve aerosol optical properties for GEMS measurements over Asia. *Remote Sens.* **2018**, *10*, 162. [CrossRef]
38. Toller, G.; Xiong, X.J.; Sun, J.; Wenny, B.N.; Geng, X.; Kuyper, J.; Angal, A.; Chen, H.; Madhavan, S.; Wu, A. Terra and Aqua moderate-resolution imaging spectroradiometer collection 6 level 1B algorithm. *J. Appl. Remote Sens.* **2013**, *7*, 073557. [CrossRef]
39. Park, S.S.; Kim, J.; Lee, J.; Lee, S.; Kim, J.S.; Chang, L.S.; Ou, S. Combined dust detection algorithm by using MODIS infrared channels over East Asia. *Remote Sens. Environ.* **2014**, *141*, 24–39. [CrossRef]
40. Lyapustin, A.; Wang, Y.; Xiong, X.; Meister, G.; Platnick, S.; Levy, R.; Franz, B.; Korkin, S.; Hilker, T.; Tucker, J. Scientific impact of MODIS C5 calibration degradation and C6+ improvements. *Atmos. Meas. Tech.* **2014**, *7*, 4353–4365. [CrossRef]

41. Sayer, A.; Hsu, N.; Bettenhausen, C.; Jeong, M.J.; Meister, G. Effect of MODIS Terra radiometric calibration improvements on Collection 6 Deep Blue aerosol products: Validation and Terra/Aqua consistency. *J. Geophys. Res. Atmos.* **2015**, *120*, 12157–12174. [CrossRef]
42. Levy, R.; Remer, L.; Kleidman, R.; Mattoo, S.; Ichoku, C.; Kahn, R.; Eck, T. Global evaluation of the Collection 5 MODIS dark-target aerosol products over land. *Atmos. Chem. Phys.* **2010**, *10*, 10399–10420. [CrossRef]
43. Gupta, P.; Levy, R.C.; Mattoo, S.; Remer, L.A.; Munchak, L.A. A surface reflectance scheme for retrieving aerosol optical depth over urban surfaces in MODIS Dark Target retrieval algorithm. *Atmos. Meas. Tech.* **2016**, *9*, 3293–3308. [CrossRef]
44. Vasilkov, A.; Qin, W.; Krotkov, N.; Lamsal, L.; Spurr, R.; Haffner, D.; Joiner, J.; Eun-Su, Y.; Marchenko, S. Accounting for the effects of surface BRDF on satellite cloud and trace-gas retrievals: A new approach based on geometry-dependent Lambertian equivalent reflectivity applied to OMI algorithms. *Atmos. Meas. Tech.* **2017**, *10*, 333–349. [CrossRef]
45. Cescatti, A.; Marcolla, B.; Vannan, S.K.S.; Pan, J.Y.; Román, M.O.; Yang, X.; Ciais, P.; Cook, R.B.; Law, B.E.; Matteucci, G. Intercomparison of MODIS albedo retrievals and in situ measurements across the global FLUXNET network. *Remote Sens. Environ.* **2012**, *121*, 323–334. [CrossRef]
46. Winker, D.M.; Pelon, J.R.; McCormick, M.P. CALIPSO mission: Spaceborne lidar for observation of aerosols and clouds. In *Lidar Remote Sensing for Industry and Environment Monitoring III*; SPIE: Bellingham, WA, USA, 2003; Volume 4893, pp. 1–11.
47. Torres, O.; Bhartia, P.K.; Sinyuk, A.; Welton, E.J.; Holben, B. Total Ozone Mapping Spectrometer measurements of aerosol absorption from space: Comparison to SAFARI 2000 ground—Based observations. *J. Geophys. Res. Atmos.* **2005**, *110*. [CrossRef]
48. Swap, R.J.; Annegarn, H.J.; Suttles, J.T.; Haywood, J.; Helmlinger, M.C.; Hely, C.; Hobbs, P.V.; Holben, B.N.; Ji, J.; King, M.D.; et al. The Southern African Regional Science Initiative (SAFARI 2000): Overview of the dry season field campaign. *S. Afr. J. Sci.* **2002**, *98*, 125–130.
49. Holben, B.N.; Eck, T.F.; Slutsker, I.a.; Tanre, D.; Buis, J.; Setzer, A.; Vermote, E.; Reagan, J.A.; Kaufman, Y.; Nakajima, T. AERONET—A federated instrument network and data archive for aerosol characterization. *Remote Sens. Environ.* **1998**, *66*, 1–16. [CrossRef]
50. Giles, D.M.; Sinyuk, A.; Sorokin, M.G.; Schafer, J.S.; Smirnov, A.; Slutsker, I.; Eck, T.F.; Holben, B.N.; Lewis, J.R.; Campbell, J.R.; et al. Advancements in the Aerosol Robotic Network (AERONET) Version 3 database–automated near-real-time quality control algorithm with improved cloud screening for Sun photometer aerosol optical depth (AOD) measurements. *Atmos. Meas. Tech.* **2019**, *12*, 169–209. [CrossRef]
51. Dubovik, O.; Smirnov, A.; Holben, B.N.; King, M.D.; Kaufman, Y.J.; Eck, T.F.; Slutsker, I. Accuracy assessments of aerosol optical properties retrieved from Aerosol Robotic Network (AERONET) Sun and sky radiance measurements. *J. Geophys. Res. Atmos.* **2000**, *105*, 9791–9806. [CrossRef]
52. Dubovik, O.; Holben, B.; Eck, T.F.; Smirnov, A.; Kaufman, Y.J.; King, M.D.; Tanre, D.; Slutsker, I. Variability of absorption and optical properties of key aerosol types observed in worldwide locations. *J. Atmos. Sci.* **2002**, *59*, 590–608. [CrossRef]
53. Eck, T.F.; Holben, B.N.; Reid, J.S.; Xian, P.; Giles, D.M.; Sinyuk, A.; Smirnov, A.; Schafer, J.S.; Slutsker, I.; Kim, J.; et al. Observations of the interaction and transport of fine mode aerosols with cloud and/or fog in Northeast Asia from Aerosol Robotic Network and satellite remote sensing. *J. Geophys. Res. Atmos.* **2018**, *123*, 5560–5587. [CrossRef]
54. Leahy, L.V.; Anderson, T.L.; Eck, T.F.; Bergstrom, R.W. A synthesis of single scattering albedo of biomass burning aerosol over southern Africa during SAFARI 2000. *Geophys. Res. Lett.* **2007**, *34*, 12. [CrossRef]
55. Haywood, J.; Francis, P.; Dubovik, O.; Glew, M.; Holben, B. Comparison of aerosol size distributions, radiative properties, and optical depths determined by aircraft observations and Sun photometers during SAFARI 2000. *J. Geophys. Res. Atmos.* **2003**, *108*. [CrossRef]
56. Mok, J.; Krotkov, N.A.; Torres, O.; Jethva, H.; Li, Z.; Kim, J.; Koo, J.-H.; Go, S.; Irie, H.; Labow, G. Comparisons of spectral aerosol single scattering albedo in Seoul, South Korea. *Atmos. Meas. Tech.* **2018**, *11*, 2295–2311. [CrossRef]
57. Dubovik, O.; Herman, M.; Holdak, A.; Lapyonok, T.; Tanré, D.; Deuzé, J.L.; Ducos, F.; Sinyuk, A.; Lopatin, A. Statistically optimized inversion algorithm for enhanced retrieval of aerosol properties from spectral multi-angle polarimetric satellite observations. *Atmos. Meas. Tech.* **2011**, *4*, 975–1018. [CrossRef]

58. Dubovik, O.; Sinyuk, A.; Lapyonok, T.; Holben, B.N.; Mishchenko, M.; Yang, P.; Eck, T.F.; Volten, H.; Munoz, O.; Veihelmann, B. Application of spheroid models to account for aerosol particle nonsphericity in remote sensing of desert dust. *J. Geophys. Res. Atmos.* **2006**, *111*. [CrossRef]
59. Torres, O.; Bhartia, P.K.; Jethva, H.; Ahn, C. Impact of the ozone monitoring instrument row anomaly on the long-term record of aerosol products. *Atmos. Meas. Tech.* **2018**, *11*, 2701–2715. [CrossRef]
60. Okada, K.; Kobayashi, A.; Iwasaka, Y.; Naruse, H.; Tanaka, T.; Nemoto, O. Features of individual Asian dust-storm particles collected at Nagoya, Japan. *J. Meteorol. Soc. Jpn. Ser. II* **1987**, *65*, 515–521. [CrossRef]
61. Okada, K.; Heintzenberg, J.; Kai, K.; Qin, Y. Shape of atmospheric mineral particles collected in three Chinese arid–regions. *Geophys. Res. Lett.* **2001**, *28*, 3123–3126. [CrossRef]
62. Li, J.; Osada, K. Water-insoluble particles in spring snow at Mt. Tateyama, Japan: Characteristics of the shape factors and size distribution in relation with their origin and transportation. *J. Meteorol. Soc. Jpn. Ser. II* **2007**, *85*, 137–149. [CrossRef]
63. Formenti, P.; Schütz, L.; Balkanski, Y.; Desboeufs, K.; Ebert, M.; Kandler, K.; Petzold, A.; Scheuvens, D.; Weinbruch, S.; Zhang, D. Recent progress in understanding physical and chemical properties of African and Asian mineral dust. *Atmos. Chem. Phys.* **2011**, *11*, 8231–8256. [CrossRef]
64. Kleipool, Q.; Dobber, M.; de Haan, J.; Levelt, P. Earth surface reflectance climatology from 3 years of OMI data. *J. Geophys. Res. Atmos.* **2008**, *113*. [CrossRef]
65. Ahn, C.; Torres, O.; Jethva, H. Assessment of OMI near–UV aerosol optical depth over land. *J. Geophys. Res. Atmos.* **2014**, *119*, 2457–2473. [CrossRef]
66. Ciren, P.; Kondragunta, S. Dust aerosol index (DAI) algorithm for MODIS. *J. Geophys. Res. Atmos.* **2014**, *119*, 4770–4792. [CrossRef]
67. Torres, O.; Decae, R.; Veefkind, P.; de Leeuw, G. OMI Aerosol Retrieval Algorithm. OMI Algorithm Theoretical Basis Document: Clouds, Aerosols, and Surface UV Irradiance. 2002; Volume 3. Available online: https://eospso.gsfc.nasa.gov/sites/default/files/atbd/ATBD-OMI-03.pdf (accessed on 27 September 2020).
68. Veefkind, J.P.; de Leeuw, G.; Durkee, P.A. Retrieval of aerosol optical depth over land using two-angle view satellite radiometry during TARFOX. *Geophys. Res. Lett.* **1998**, *25*, 3135–3138. [CrossRef]
69. Veefkind, J.P.; de Leeuw, G.; Stammes, P.; Koelemeijer, R.B. Regional distribution of aerosol over land, derived from ATSR-2 and GOME. *Remote Sens. Environ.* **2000**, *74*, 377–386. [CrossRef]
70. Torres, O.; Bhartia, P.K.; Herman, J.R.; Sinyuk, A.; Ginoux, P.; Holben, B. A long-term record of aerosol optical depth from TOMS observations and comparison to AERONET measurements. *J. Atmos. Sci.* **2002**, *59*, 398–413. [CrossRef]
71. Remer, L.A.; Kleidman, R.G.; Levy, R.C.; Kaufman, Y.J.; Tanré, D.; Mattoo, S.; Martins, J.V.; Ichoku, C.; Koren, I.; Yu, H.; et al. Global aerosol climatology from the MODIS satellite sensors. *J. Geophys. Res. Atmos.* **2008**, *113*. [CrossRef]
72. Tanré, D.; Remer, L.A.; Kaufman, Y.J.; Mattoo, S.; Hobbs, P.V.; Livingston, J.M.; Russel, P.B.; Smirnov, A. Retrieval of aerosol optical thickness and size distribution over ocean from the MODIS airborne simulator during TARFOX. *J. Geophys. Res. Atmos.* **1999**, *104*, 2261–2278. [CrossRef]
73. Chu, D.A.; Kaufman, Y.J.; Remer, L.A.; Holben, B.N. Remote sensing of smoke from MODIS airborne simulator during the SCAR–B experiment. *J. Geophys. Res. Atmos.* **1998**, *103*, 31979–31987. [CrossRef]
74. Hsu, N.C.; Jeong, M.J.; Bettenhausen, C.; Sayer, A.M.; Hansell, R.; Seftor, C.S.; Huang, J.; Tsay, S.C. Enhanced Deep Blue aerosol retrieval algorithm: The second generation. *J. Geophys. Res. Atmos.* **2013**, *118*, 9296–9315. [CrossRef]
75. Lee, J.; Kim, J.; Song, C.H.; Ryu, J.H.; Ahn, Y.H.; Song, C.K. Algorithm for retrieval of aerosol optical properties over the ocean from the Geostationary Ocean Color Imager. *Remote Sens. Environ.* **2010**, *114*, 1077–1088. [CrossRef]
76. Choi, M.; Kim, J.; Lee, J.; Kim, M.; Park, Y.-J.; Jeong, U.; Kim, W.; Hong, H.; Holben, B.; Eck, T.F.; et al. GOCI Yonsei Aerosol Retrieval (YAER) algorithm and validation during the DRAGON-NE Asia 2012 campaign. *Atmos. Meas. Tech.* **2016**, *9*, 1377–1398. [CrossRef]
77. Chu, M.; Dodd, J. Examination of Radiometric Deviations in Bands 29, 31, and 32 of MODIS Collection 6.0 and 6.1. *IEEE Trans. Geosci. Remote Sens.* **2019**, *57*, 5790–5798. [CrossRef]
78. Sorek-Hamer, M.; Kloog, I.; Koutrakis, P.; Strawa, A.W.; Chatfield, R.; Cohen, A.; Ridgway, W.L.; Broday, D.M. Assessment of $PM_{2.5}$ concentrations over bright surfaces using MODIS satellite observations. *Remote Sens. Environ.* **2015**, *163*, 180–185. [CrossRef]

79. Bilal, M.; Nichol, J.E.; Spak, S.N. A new approach for estimation of fine particulate concentrations using satellite aerosol optical depth and binning of meteorological variables. *Aerosol Air Qual. Res.* **2016**, *17*, 356–367. [CrossRef]
80. Song, Z.; Fu, D.; Zhang, X.; Han, X.; Song, J.; Zhang, J.; Wang, Z.; Xia, X. MODIS AOD sampling rate and its effect on $PM_{2.5}$ estimation in North China. *Atmos. Environ.* **2019**, *209*, 14–22. [CrossRef]